Magnetic fabric of Bengal fan sediments: Holocene record of sedimentary processes and turbidite activity from the Ganges-Brahmaputra river system

Eva Moreno, Fabien Caroir, Léa Fournier, Kelly Fauquembergue, Sébastien Zaragosi, Ronan Joussain, Christophe Colin, Marie-Madeleine Blanc-Valleron, François Baudin, Thibault de Garidel-Thoron, et al.

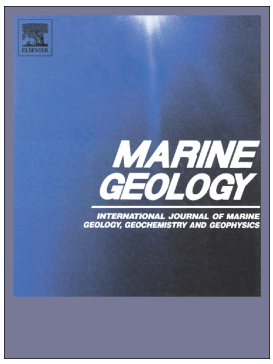

Magnetic fabric of Bengal fan sediments: Holocene record of sedimentary processes and turbidite activity from the Ganges-Brahmaputra river system

Eva Moreno, Fabien Caroir, Lea Fournier, Kelly Fauquembergue, Sébastien Zaragosi, Ronan Joussain, Christophe Colin, Marie-Madeleine Blanc-Valleron, François Baudin, Thibault de Garidel-Thoron, Jean Pierre Valet, Franck Bassinot

PII: S0025-3227(20)30235-8

DOI: https://doi.org/10.1016/j.margeo.2020.106347

Reference: MARGO 106347

To appear in: *Marine Geology*

Received date: 22 May 2020

Revised date: 8 September 2020

Accepted date: 15 September 2020

Please cite this article as: E. Moreno, F. Caroir, L. Fournier, et al., Magnetic fabric of Bengal fan sediments: Holocene record of sedimentary processes and turbidite activity from the Ganges-Brahmaputra river system, *Marine Geology* (2020), https://doi.org/10.1016/j.margeo.2020.106347

Magnetic fabric of Bengal fan sediments: Holocene Record of sedimentary processes and turbidite activity from the Ganges-Brahmaputra river system

Eva Moreno[1], Fabien Caroir[2], Lea Fournier[3], Kelly Fauquembergue[3], Sébastien Zaragosi[3], Ronan Joussain[4], Christophe Colin[4], Marie-Madeleine Blanc-Valleron[5], François Baudin[6], Thibault de Garidel-Thoron[7], Jean Pierre Valet[8], Franck Bassinot[9]

1. Laboratoire d'Océanographie et du Climat: Expérimentations et approches numériques, UMR 7159 CNRS / IRD / Sorbonne Université/MNHN/IPSL. Boîte 100 - 4, place Jussieu 75252 Paris cedex 05, France.
2. Université Lille, CNRS, Université Littoral Côte d'Opale, UMR 8187, LOG, Laboratoire d'Océanologie et de Géosciences, F 59000 Lille, France.
3. UMR CNRS 5805 EPOC - OASU - Université de Bordeaux, Allée Geoffroy Saint-Hilaire - CS 50023 - 33615 Pessac cedex – France.
4. Université Paris-Saclay, CNRS, GEOPS, 91405, Orsay, France.
5. CR2P, Muséum National d'Histoire Naturelle, UMR 7207, 43 Rue Buffon - CP56, Paris, France.
6. Sorbonne Université, ISTeP - Institut des Sciences de la Terre Paris, 4 place Jussieu, CP 117, 75005 Paris.
7. Aix-Marseille Université, CNRS, IRD, Coll. de France, INRAE, CEREGE, Technopôle de l'Arbois - BP80 - 13545 Aix-en-Provence cedex 04, France.
8. Institut De Physique Du Globe De Paris, 1, Université de Paris, 1 rue Jussieu - 75238 Paris cedex 05, France.
9. Laboratoire des Sciences du Climat et de l'Environnement, LSCE/IPSL, CEA-CNRS-UVSQ, Université Paris-Saclay, F-91191, Gif-sur-Yvette, France.

Keywords: Bengal fan, Holocene, turbidite activity, magnetic fabric, magnetic mineralogy.

1 Introduction

The anisotropy of magnetic susceptibility (AMS) technique is a useful method to study the sedimentary fabric of marine and lakes sediment. Magnetic fabric derived from AMS analyses reflect the shape and preferred alignment of sedimentary particles during deposition under the presence of bottom-currents. Therefore, AMS has been successfully used to identify bottom currents directions in different environments including contourites, submarine fan, fluvial and delta environment (Abdeldayem, 1999; Beckers et al., 2016; Felletti et al., 2016; Ge et al., 2012; Kissel et al., 1998; Parés et al., 2007; Tamaki et al., 2015). The AMS technique is particularly powerful in combination with grain-size measurements as these two properties enable to differentiate between high depositional energy environments like turbidite or mass-transport deposits composed of coarse to fine-grained terrigenous detritus and hemipelagic deposits built by settling (Abdeldayem, 1999; Joseph et al., 1998; Kissel et al., 1997; Kissel et al., 1998; Meissl et al., 2011). These techniques have also been

successfully used to identify major seismic events in lake (Carrillo et al., 2008) and marine environments (Campos et al., 2014; Campos et al., 2013).

In this article we study the magnetic fabrics of Holocene sediments located on the eastern levee of the Bengal Fan Active Channel that have recorded several turbidite deposits (Figure 1). This channel is fed by the Ganges-Brahmaputra (G-B) river system and has been subjected to intense turbidite activity for the past 14.5 ka cal. BP (Weber et al., 1997). Here we focus on a continuous and unique core recording more than 200 silty-sandy to fine silt turbidity sequences that have been deposited during the past 9.8 ka cal. BP under extremely high sedimentation rates (Fournier et al., 2017). The aim of this work is to: (1) investigate the anisotropy of magnetic susceptibility (AMS) at high resolution; (2) search for consistent trends in the AMS properties of the levee turbidites; (3) determine the relationship of the magnetic fabric with the grain-size and the mineralogical properties of previously studied turbidite layers (Fournier et al., 2017).

2 Geological setting of the Bengal Fan

The Bengal Fan is the largest submarine fan in the world, with a length of about 3000 km, a width of about 1000 km and a thickness that can reach 16.5 km (Curray et al., 2003). Terrigenous material is mainly supplied by the G-B Rivers (Curray et al., 2003) with minor contributions from other rivers in Bangladesh, India and Burma (Liu, J. P. et al., 2019). The annual sedimentary discharges of the G-B Rivers are estimated at around 1×10^9 t/y which is the largest of the world (Milliman, 2001). However, the hydrological cycle in the G-B basin is governed by the summer monsoon and consequently, the river runoff in the G-B is highly seasonal: about 90% of Ganges sediments and more than 80% of Brahmaputra sediments are transferred from June to September (Unger et al., 2003).

Riverine sediments are transferred to the deep-sea fan as turbidity currents in channel-levee systems that have been developed from G-B river mouth to the equatorial sea area. This turbidite system is known as the Bengal Fan (Curray et al., 2003). Nowadays, there is only one active channel connected by the submarine canyon “Swath of No Ground” (SoNG) (Figure 1) (Curray et al., 2003).

The construction of this channel began around 14.5 ka cal. BP (Weber et al., 1997) and was followed by intense turbidite activity up to 9.2 ka cal. BP which resulted in large sediment thickness. Thus, at the site of the MD12-3417 and MD12-3418 cores that will be studied in this work, the sedimentation rate between 9.8 and 9.2 ka cal. BP was unusually high, between 3.5 and 9.5 cm/year due to almost continuous turbidite inputs. This turbidite activity continued during the sea level rise and in the rest of the Holocene but in a less intense way so that the sedimentation rate was reduced to 0.02-0.18 cm/year from 9.2 ka cal. BP, being still very high (Fournier et al., 2017).

Two main processes have been documented to influence the construction of the SoNG system: post-glacial sea-level forcing and hydrological forcing through the monsoon. According to previous works (Fauquembergue et al., 2019; Fournier et al., 2017; Joussain et al., 2017; Weber et al., 1997), turbidite sedimentation in the Active Channel was clearly linked with global sea-level rise in presence of higher precipitation related to an enhancement of the Indian summer monsoon during early Holocene. The global sea level from 14.5 to 9.2 ka cal. BP is between −95 and −20 m with respect to present day according to the global sea-level curve (Lambeck et al., 2014). As consequence, there was good a fluvial connection with the SoNG leading to sediments largely bypassing both delta and shelf margin and being exported to the Bengal Fan. Additionally, Indian monsoon precipitation fluctuated significantly during the Holocene. Numerous studies showed that the Indian summer monsoon was strengthened during the early Holocene (Gupta et al., 2005; Joussain et al., 2017; Kumar et al., 2019; Thamban et al., 2007) followed by a gradual weakening over the past 8 ka with a more or less stable dry phase beginning ~5 ka BP that coincides with the onset of an arid Indian phase (Sharma et al., 2004). As a result, the G-B sediment discharge was enormously increased during early Holocene (Goodbred and Kuehl, 2000). Results estimated that the mean sediment load of the G-B river system was 2 times higher (~2.3×10^9 t/year) between 11 and 7 ka cal. BP, than for present time (Goodbred and Kuehl, 2000).

3 Studied cores and previous works

Calypso giant-piston core MD12-3417 (16°30.03′N; 87°47.82′E; water depth: 2564 m, 39.77 m long) and the Calypso square (CASQ) gravity core MD12-3418CQ located at the same site (16°30.27′N;

87°47.92′E; water depth: 2557 m, 8.52 m long) were taken during the MD191/MONOPOL expedition (Bassinot and Beaufort, 2012) of the French R/V Marion Dufresne in 2012 (Figure 1). The cores are stored in the marine collection of the *Museum national d'Histoire naturelle* from Paris (France) under the inventory numbers MNHN-GS-MD12-3417 and MNHN-GS-MD123418CQ.

These cores were taken on the eastern levee of the active channel. Two previous studies of these cores have been already conducted to constrain the controlling factors implied in turbidite activity of the active channel (Fournier et al., 2017) and the link between Indian summer monsoon rainfall intensity and weathering of the G -B river basin (Joussain et al., 2017) during the Holocene.

Fournier et al. (2017) used a composite record, generated by splicing core MD12-3418CQ with the base of core MD12-3417 (11-40 m). This composite record was achieved by matching the X-ray fluorescence (XRF) high-resolution data of both cores and then converting core MD12-3417 depth scale into core MD12-3418C depth scale. This composite record will be subsequently referred to MD17&18. Based on thirteen ^{14}C dates (Fournier et al., 2017), the composite core MD17&18 represents a continuous sedimentary record for the past 9.8 ka cal. BP (Figure 2).

4 Sampling and methods

4.1 Anisotropy of magnetic anisotropy (AMS)

AMS measurements were carried out at the *Institut de Physique du Globe* (IPGP) in Paris using an AGICO Kappabridge KLY3 susceptibilimeter (with $2x10^{-8}$ SI sensitivity) and an alternating field of 300 Am^{-1} intensity at 875 Hz frequency.

A total of 564 discrete samples were obtained through continuous sub-sampling by pressing 8 cm3 plastic cubes. All samples from the MD12-3417 core were taken from the working halves. The cubes were oriented along the Z axis of the core with the arrow pointing to the top of the section. The average sampling interval is 5 cm, varying from a maximum of 20 cm in the hemipelagic sediment to a minimum of 2 cm in turbidite sequences. Core CASQ MD12-3418 core has a square section (0.25x0.25 m²). The sediment was first sub-sampled on-board in 5 equivalent "half-sections" using

PVC U-channels 6 cm wide and 5 cm deep. The cubes for the AMS were then taken in one of these 5 "half-sections" and oriented in the same way as for the MD12-3417 core.

The AMS is determined from a second order symmetric tensor. The Eigen vectors define the maximum (K_1), intermediate (K_2) and minimum (K_3) axes of the susceptibility ellipsoid that represents the global anisotropy resulting from the individual grain shapes and their alignment within the sample. It depends also on the crystallographic axes (Tarling and Hrouda, 1993).

The *magnetic lineation* (K_1/K_2) and *magnetic foliation* (K_2/K_3) have been used to describe the magnetic fabric. The term magnetic lineation (L) may be used to characterize the intensity of the linear-parallel orientation, while the magnetic foliation (F) characterizes the intensity of the planar-parallel orientation of minerals in a rock (Tarling and Hrouda, 1993). When plotted on Flinn diagrams they enable to determine whether the fabric is oblate (F>L) or prolate (F<L). The shape parameter T ($T=[2\ln K_2-\ln K_1-\ln K_3)/(\ln K_1-\ln K_3]$) fluctuates between 1 and -1. When T is close to 1 or positive, the ellipsoid is oblate, when T is negative, then the ellipsoid is prolate. If T = 0, then the ellipsoid is neutral or spherical. The Pj parameter defines the corrected degree of anisotropy, indicates the intensity of the preferred orientation of magnetic minerals in a rock, high values represent a strong degree of anisotropy ($Pj= \exp\sqrt{2[(\eta 1-\eta m)2+(\eta 2-\eta m)2+(\eta 3-\eta m)2)]}$ with $\eta 1=\ln K_1$; $\eta 2=\ln K_2$; $\eta 3=\ln K_3$). Lastly, we used the inclination of the K_3 direction ($IncK_3$) which indicates the tilt of the short axis K_3.

4.1.1 Anhysteretic Remanent Magnetization (ARM)

In addition, the Anhysteretic Remanent Magnetization (ARM) was measured on 78 samples between 770 cm and 2051 cm (composite core depth) with a resolution of 5 to 20 cm depending on the interval. The ARM was imparted in a 50 µT steady field combined with a linearly decaying alternating field of 80 mT using a Schonstedt demagnetizer that was equipped for that purpose.

Following the acquisition, the ARM measurements were performed on a 2G cryogenic magnetometer at the IPGP. Thereafter, ARM results were divided by magnetic susceptibility (ARM/K). Indeed, the ARM/k ratio is inversely related to the grain-size of magnetite and titano-magnetite (Banerjee et al.

1981; King et al. 1982). These results are shown in the complementary Figure S3 compared with the percentage of sands and silts.

4.2 Low temperature measurements

Low-temperature isothermal remanence magnetizations (LT-SIRM) were made in core MD17&18 using a Quantum Design Magnetic Property Measurement System (MPMS2) SQUID magnetometer at the IPGP in Paris (France). For these analyses, we selected a small amount of sediment (a few milligrams) from the hemipelagic intervals and turbidites of Unit 1 and 2. The sediment was dried, ground and inserted within gelatin capsules for measurements in the MPMS. Two different LT-SIRM experiments were performed.

-Low-temperature (10 K) Saturation Isothermal Remanent Magnetization (SIRM) were imparted after cooling in a 2.5 T field (field cooling, FC) and in a zero field environment (zero field cooling, ZFC). The SIRM was measured in approximately zero field at 5 K intervals up to 300 K.

-SIRM magnetization was imparted at room temperature (RT-SIRM) by applying a maximum field of 2.5 T at 300 K followed by continuous cooling in zero field to 10 K and subsequent continuous warming back to 300 K at 5-K intervals.

4.3 Sedimentological analyses

The sedimentological analyses performed include the high resolution analysis of the chemical elements by X-ray fluorescence (XRF) and the analysis of the grain-size and $CacO_3$ content. XRF and grain-size results have already been published in Fournier et al. (2017).

4.3.1 X-ray images, Scopix

X-ray images were taken using the Scopix X-ray imaging system from the PAACS platform at the EPOC laboratory. The acquisition was done on 1 cm thick aluminum plates taken from the core half-sections. This method optimizes the resolution and homogenizes the X-ray response over the entire core.

X-ray radiography makes it possible to observe variations in the density and nature of the sediment. The images obtained are based on a grey scale. Denser sediment tends to absorb more x-rays, resulting

in a darker shade of grey. On the contrary, a sediment that is not very dense, or with a coarser grain-size, will give a lighter shade of grey. Thus, this tool makes it possible to visualize the structure and organization of sediments and to identify sedimentary processes and it can be used to recognize facies such as turbidites (Migeon et al. 1999).

4.3.2 Carbonate content

A total of 148 $CaCO_3$ analyses were performed using a carbonate bomb at MNHN (50 measurements) and rock-Eval at ISTeP (98 measurements) using a method devoted to recent sediments (Baudin et al., 2015). These data were subsequently used to calibrate the Ca values measured by XRF using a linear equation (Pearson correlation=0.89), this linear equation was then applied to the continuous XRF record to derive a very high-resolution $CaCO_3$ curve.

5 Results

5.1 Down-core fluctuations in XRF data and grain-size parameters

Figure 2 shows the selected geochemical parameters analyzed by XRF together with the $CaCO_3$ content and the median grain-size (d50) of the MD17&18 composite core as function of depth. In addition, in this figure, the sedimentation rate and radiocarbon data can also be seen. Age mode, Ti/Ca and Zr/Rb ratios and the d50 data were already published (Fournier et al., 2017). the Si/Al ratio are published now for the first time. In this article, the XRF-ratios were expressed as logarithms of ratios of abundances as they provide the most robust record of relative chemical changes (Weltje and Tjallingii, 2008).

The ln(Zr/Rb) ratio (Calvert and Price 1983; Dypvik and Harris, 2001) and ln(Si/Al) ratio (Liu et al. 2018) can be interpreted to indicate grain-size variations. Due to the relative high content of sand and coarse silt within the turbidite layers, water content can increase and reduce element intensities (Boyle et al. 2015), specially for the lighter elements Al and Si (Tjallingii et al. 2007). However, the use of relative variations using element ratio makes it possible to minimize the influence of sediment porosity and water content. In fact, it can be seen in Figure 2 that the variations of the ln(Zr/Rb) and ln(Si/Al)

ratios are nearly identical to the variations of d50 and that these vary in phase and with similar amplitudes to the grain-size.

Besides, the ln(Ti/Ca) ratio is commonly used to compare the siliciclastic fraction (Ti) and the biogenic Ca fraction (Kuhn et al. 2015; Revel et al. 2015; ; St-Onge et al.2007) . However, in core MD17&18, microscopic observations indicate that $CaCO_3$ is mainly composed of detrital calcite (Fournier et al., 2017). Detrital calcite was more concentrated in turbidite sequences and the ln (Ti/ Ca) ratio was used to identify fine-grained turbidite sequences.

Based on the previous work by Fournier et al. (2017), core MD17&18 was divided in two Units depending on the intensity of turbidite activity:

- Unit 1 that covers the age interval between 9.862±2.00 ka cal. BP and 9.226 ±1.40 ka cal. BP (1089-4053 cm in composite depth) and includes only core MD12-3417. Several turbidite levels can be easily recognized from the increase in median grain-size, ln(Zr/Rb) and ln (Si/Al) ratios and the decrease in the ln(Ti/Ca) ratio. The $CaCO_3$ percentage of the sediment is around 6%.
- Unit 2 goes from 9.226 ±1.40 ka cal. BP to the present (0-1088 cm) and includes the entire MD12-3418CQ core (0-824 cm) and a small interval of core MD12-3417 (831-1088 cm). In this unit, only one peak is visible in the median grain-size and the ln(Zr/Rb) and ln(Si/Al) ratios between 120 and 155 cm similarly to those observed in Unit 1. The rest of the interval has a median grain-size of 10µm. However, several fine-grained turbidites were recognized from the ln(Ti/Ca) ratio. The percentage of $CaCO_3$ is around 3%.

5.2 Down-core fluctuations in AMS parameters

The down-core fluctuations of bulk magnetic susceptibility (Km), lineation (L), foliation (F), corrected degree of anisotropy (Pj), shape parameter (T), inclination of the AMS K_3 axes and percentage of silts and sands of core MD17&18 have been reported in Figure 3. The turbidite level between 120 and 155 cm was already studied by AMS in a previous study (Tanty et al., 2016). Additional measurements were performed on new samples.

Bulk magnetic susceptibility (Km) is usually considered as a proxy for rock composition. In core MD17&18, Km fluctuated in parallel to the percentage of silts and sands. The Km value of core MD17&18 range between 100-700x10^{-6} SI. The mean susceptibilities of 275±38x10^{-6} SI for Unit 1 and 267±43x10^{-6} SI for Unit 2 outside the turbidite layers are relative similar and they correspond to values of paramagnetic minerals (<300x10^{-6}SI) like clays and phyllosilicates (e.g., Tarling and Hrouda, 1993). However, during the turbidite sequences of Unit 1, the Km increase highly, mean values were 364±93x10^{-6} SI with a maximum of 671x10^{-6} SI which reflect either a stronger magnetic concentration or changes in magnetic mineralogy.

The lineation is very low in the entire record (L<1.06) and shows excursions associated with some but not all the turbidite layers. In Unit 1, the highest L values correspond to either thick turbidite levels or levels with larger sediment grain-size. In Unit 2, many more high L values are characterized by a slight increase in sediment grain-size, except at level 120-155 cm.

Besides, F and Pj are extremely high (up to 1.35 for Pj and to 1.3 for F) and with similar downcore patterns, which indicates that the degree of anisotropy is controlled by foliation. In Unit 1, the values are higher than in Unit 2, but there is no clear increase with depth and therefore compaction has no impact. However, F and Pj show a clear increase in turbidite levels of both Units 1 and 2. In Unit 1, the increase is accompanied by a larger magnetic susceptibility.

The inclination of the K_3 axes is close to 90°, thus, normal to the bedding plane. This corresponds to classic magnetic fabric of sediments that were deposited in still water on an horizontal plane. However, several turbidite layers with lower IncK_3 indicate that grains were tilted by more than 10-20° and even sometimes by more than 60°. The largest deviations (Inc=60-75°) were observed between 1180 and 1350 cm (section XI of core MD12-3417). This behavior is not linked to a different deposition mechanism but was rather caused by an important perturbation of the sedimentary structure. Indeed, in this interval, there is one of the thickest turbidites in the core characterized by a very high amount of sand and a high water content. This feature, was likely the cause of non-optimal coring recovery, which disturbed the sedimentary structure and explain the unusual AMS values in section 11 of core MD12-3417. This perturbation is observed in the X-ray photographs (Figure S2,

supplementary data). One other turbidite has a deviation of more than 30° at the 3140-3180 cm interval but for the rest, the dips in the inclination of K_3 have an order of magnitude that is typical of turbidite currents composed of fine sands and silts (Park et al., 2013).

The difference in magnetic fabric between turbidite levels and hemipelagic sediment of Units 1 and 2 can be easily observed on the Jelinek (Pj /T) and Flinn (F/L) diagrams (Figure 4). The T shape parameter indicates an oblate sedimentary fabric in most points from Units 1 and 2. Several samples, especially from turbidites, are characterized by T values that are close to zero and even negative indicating a triaxial to prolate type fabric. In Unit 2 which is supposedly associated with less turbidite activity, the lineation (L), foliation (F) and the corrected degree of anisotropy (Pj) have lower values than in Unit 1, but the turbidite sequences remain clearly distinguished. Figure 4 also shows the Pj-Km and Pj-d50 diagram in order to investigate the influence of mineralogical and grain size in AMS. These diagrams didn't show a clear linear correlation between the highest degree of anisotropy values and the highest Km/d50 values. These results indicate that Pj values are not influenced by mineralogical/grain size variations and likely reflect changes in hydrodynamic conditions during turbidite deposition.

The stereographic plots of the principal K_1 and K_3 susceptibility axes are shown in Figure 5. The plots are divided into two types, turbidites and hemipelagic sediments, based on the median grain-size for Unit 1 and Ti/Ca ratios for Unit 2.

In Unit 1, The K_1 axes are broadly girdle-distributed on the bedding plane, whereas the K_3 axes are subvertical in almost all samples reflecting a well-developed sedimentary fabric. The K_1 axes of Unit 2 present also girdle-distributed but with a weak clustering. The K_3 axes are subvertical and slightly tilted towards the horizontal plane. This weak clustering could indicate a paleocurrent imprint. However, as the samples were not palaeomagnetically oriented, we cannot determinate absolute paleocurrent direction.

5.3 Low temperature SIRM

Low-temperature SIRM curves for three selected samples corresponding to Unit 1, Unit 2 and the turbidite located ~ 1733 cm are shown in Figure 6. All samples display a similar behavior which suggests that they share similar magnetic mineralogy. We note that the turbidite sample at 1733 cm has much higher SIRM values indicating that it was enriched in magnetic minerals.

A sharp Verwey transition at ~ 120K due to magnetite is present in both RT-SIRM and ZFC-FC curves of all samples. The RT-SIRM curves are characterized by a humped shape in both cooling and warming curves. The cooling curve shows first an increase that reaches a maximum at around 175–200 K, and then a strong decrease ahead the Verwey transition. Below 90K, the remanence continues to slightly increase to 10K. The RT-SIRM cooling and warming curves are reversible below 90K. The total lost remanence after warming back at 300K is between 6% for the turbidite at 1733 cm and 20% for sample at 830 cm (Unit 2). This behavior might suggest the presence of maghemite (Özdemir and Dunlop, 2010) or/and goethite (Taylor et al., 2014) but the RT-SIRM warming and cooling curves and their first derivatives (not shown) display a transition at circa 260K which corresponds to the Morin transition of hematite (Özdemir et al., 2008).

Finally, in the FC-ZFC experiments both the FC and ZFC curves show a gradual loss of remanence during warming. The FC values lie between 30% and 60% above the ZFC values at 10K. They remain well separated throughout the experiment and converge at 300 K. Similar behavior has been observed in loess and paleosols and suggest the presence of goethite (Taylor et al., 2014).

6 Discussion

6.1 Changes in deposition

The AMS results obtained in this study revealed a tight relationship between magnetic fabric and turbidite activity. As observed in Figure 3 and Figure 4, the turbidite sequences are characterized by a very high degree of anisotropy (Pj) and foliation (F) in both Units 1 and 2. The magnetic fabric shows also a higher lineation (L) and dips in the inclination of the K_3 axes between 15° and 25° for several but no all turbidites (Figure 3).

In order to better show the relationship between the magnetic fabric and the sedimentary structure, we have made a zoom on one of the thickest turbidites located in section 25 of core MD12-3417 between 3600 and 3670 cm depth which correspond to 3665-3749 cm of the composite depth (Figure 7).

Downcore X-ray radiography makes it possible to distinguish changes in grain-size and sedimentary structures with lighter shade of grey levels corresponding to a coarse-grained turbidite sequence. This sequence is characterized by parallel sub-horizontal, cross laminations and oblique laminations. These structures were also observed in thin section of other coarse-grained turbidites and are cut by fluid escapes structures as convolute laminations or pillars, (Fournier et al., 2017).

Vertical variations in the magnetic fabric parameters reflect these changes in sedimentation conditions. Parameters Pj, L and Km show higher values in the turbidite sequences and $IncK_3$ shows deviations of up to 20° from vertical. It is interesting to note that the variations in AMS parameters are not necessarily in phase along the turbidite sequences and that L, although increasing, is still very low.

Thus, the most significant results are the unusually high levels of Pj and F in turbidites, both the coarse-grained turbidites from Unit 1 but also the fine-grained turbidites of Unit 2 (Figure 4). These turbidites are terrigenous mainly composed by quartz, phyllosilicates (muscovite and clinochlore), detrital calcite and feldspars (Figure S1).

The fluctuations in Pj and F could be explained by changes in grain-size and/or composition related to changes in depositional conditions, influx materials and or/ in environmental changes.

However, as we mentioned above, even though the turbidites, especially the coarse-grained ones in Unit 1, have higher Pj values, there is no linear correlation between the Pj and Km/d50 values (Figure 4). This is especially the case in Unit 2, where turbidite levels are fine-grained and Km are relative low, and nevertheless, Pj values are much higher than hemipelagic sediments.

Besides, the high Pj values observed in our study could be explained by the presence of flattened phyllosilicates that are strongly anisotropic. Indeed, the selected samples measured by X-ray diffractometry (Figure S1) indicates an important contribution of muscovite and clinochlore, a mineral of the chlorite family. The mean degree of anisotropy of these minerals is Pj=1.15 (Martín-Hernández

and Hirt, 2003), in the range of the mean Pj values of Unit 2 but lower than the mean Pj values of Unit 1 (Figure 4). Therefore, the presence of these minerals is not sufficient to explain the extremely high values of Pj observed in core MD17&18.

An alternative cause of this extremely high Pj values could be high deposition rates. During consolidation, the weight of the sediment column, compress and compact the sediment. In hemipelagic sediments with relative low sedimentation rates, consolidation increase gradually with depth. With increasing vertical burial load at depth, clay mineral particles rotate to form horizontal face-to-face contacts, accompanied by simultaneous dewatering and porosity reduction The effect of this process on the microstructure of the sediment is the formation of a fabric characterized by a well-defined horizontal foliation plane and strong degree of anisotropy (Kawamura and Owaga 2004; Maffione and Morris 2017).

The sharp increase of the anisotropy degree in the turbidite sequences resembles the pattern expected for "apparent overconsolidation", whereby the sediments appear more consolidated than expected by simple burial for a given depth, and therefore the degree of anisotropy is greater (Schwehr et al., 2006; Maffione and Morris 2017). Furthermore, because turbidite sequences are deposited so quickly, they are free from the effects associated with bioturbation (Figure 7 and Figure S2, complementary data). Indeed, previous works have indicated that bioturbation can have effects in the AMS by scattering the direction of the principal susceptibilities axes (Ellwood, 1984; Bradák and Kovács, 2014).

The high sedimentation rate plays an important role in explaining the high Pj values observed in the MD17&18 core, although, as can be seen, the relationship between the degree of anisotropy and the sedimentation rate is not linear. According to the age model, the sedimentation rate decreases sharply at 2840 cm, from 9.5 cm/yr to 3.5 cm/yr, but this does not affect the Pj values. It should be remembered however that these sedimentation rates are exceptional in marine sediments and there may be a threshold effect. In addition, turbidites are instantaneous events and the deposition of each single turbidite pulse can be faster than the estimated average sedimentation rates.

Such high Pj and/or F values in turbidite sequences in marine sediments have been observed elsewhere in rapid sediments deposits, for example, sediments from Bermuda Rise, northern California (Joseph et al., 1998) and mass transport deposits (MTD) from Ursa Basin, northern Gulf of Mexico (Meissl et al. 2011). Besides, Tanty et al. (2016) investigated de AMS properties of four turbidites layers with different environmental conditions and different thickness. The results showed that the highest values in the degree of anisotropy were observed in the thickest turbidite (174 cm) in core MD98-2194 located in the Okinawa trough.

We have compared the Pj results from core MD17&18 with Pj values obtained in turbidites (Joseph et al.1998), MTD (Meissl et al. 2011) and Pj values obtained from hemipelagic sediments with low sedimentation rates (Chen et al., 2017). Turbidites and MTD sediments have higher Pj than hemipelagic sediments, but the degree of anisotropy in core MD17&18 is by far strongest (Figure 8) than in all the core samples.

This suggests that the increase in Pj during the turbidite sequences in core MD17&18 reflects a greater compaction of sedimentary structure probably due to very high sedimentation rates. MTD sediments also show strong Pj values that was interpreted as an additional compaction imposed by fast deposition (Meissl et al., 2011). Higher compaction results in a flattening of the sedimentary magnetic fabric with the K_3 axis becoming shorter and an increase in shape parameters such as Pj and F. It should also be considered that overlying the "compaction" effect, mineralogy and particle size changes play a secondary role.

6.2 Changes in sediment sources

The low-temperature measurements performed on selected samples indicated that the magnetic mineralogy is dominated by magnetite, hematite and goethite. These minerals commonly occur at concentrations less than 1 % in sediments and are therefore difficult to determine using classical mineralogical techniques like X-ray diffraction (Zhang et al., 2007). Magnetite, hematite and goethite have been identified in a ~7 Ma old sedimentary sequence of the Bengal Fan using rock-magnetic properties (Abrajevitch et al., 2009). Magnetite is the most common magnetic mineral found in

sediments. The strong correlation between Km and sediment grain-size is indicative of its detrital origin, carried by the G-B river system, the main source of detrital sediments during the Holocene (Joussain et al., 2017; Lupker et al., 2013). However, although the Km signal is mainly controlled by detrital inputs from the G-B system, the Km signal can be also be influenced by diagenetic processes. Under anoxic conditions, iron oxides can be reduced by hydrogen sulfide (H_2S) to form pyrite (FeS_2) (Philips et al. 2017; Liu, Fike, et al. 2019) resulting in decreased Km values. A recent study indicates that this process can be regulated by major changes in sedimentation rate (Liu, Fike, et al. 2019) such as those observed in core MD17&18.

However, in a recent study based on sulphur speciation and isotope ratios of core MD161/29 (Volvoikar et al. 2020) collected near core MD17&18 (Figure 1) no dominant influence of diagenesis on km values could be observed. As in the case of our study, the km values mainly reflect sediment inputs from the rivers G-B.

Due to its strong magnetic moment magnetite dominates Km, but goethite, hematite and phyllosilicates have also low to medium magnetic susceptibilities that can contribute to the global signal in presence of low magnetite concentration.

The turbidite sequences have higher Km values which indicates an increase in the concentration of magnetite and the Anhysteretic Remanent Magnetization (ARM) to magnetic susceptibility ratio (ARM/k) as well as the hysteresis parameters reveal an increase in the magnetite grain-size within the youngest coarse-grained turbidite located between 120 and 155 cm (Tanty et al., 2016). Similar results were found in other turbidite sequences from core MD17&18 (Moreno et al., 2014; Figure S3, supplementary data). Summarizing the turbidite layers are characterized by higher terrigenous grain-size, higher magnetite concentration and higher magnetite grain-size.

A previous study (Suganuma et al., 2009) suggests that the input of magnetite in sediments from the Bengal Fan is controlled by the intensity of the Asian summer monsoon. Stronger monsoon yields a northwestward expansion of the area of precipitation in the Himalayas and the northern Indian subcontinent. This process generates an expansion of the soil area which increases the pedogenic

activity in the G-B catchment area and in turn the input of magnetite in the Bengal Fan (Suganuma et al., 2009). The highest Km values occurred during Unit 1 at the beginning of the Holocene, when monsoon intensity was at its highest. Similar results were observed in the clay assemblage and the chemical weathering proxies of MD17&18 sediments reconstructed from major element concentrations (Joussain et al., 2017). This study demonstrated that the input of detrital material from the highlands was more important during the early-middle Holocene (9.8–6 ka cal. BP) whereas they mainly originated from the Indo-Gangetic plain thereafter.

7 Conclusions

The magnetic fabric of the turbidite sequences in core MD17&18 is mainly characterized by an increase in the Pj parameter. This increase occurs not only in the coarse-grained turbidites of Unit 1, but also in the fine turbidites of Unit 2, hardly recognizable in the grain-size parameters. The Pj values were extremely high (1.028-1.332) in Unit 1 between 9.3 and 9.2 ka cal. BP. During these 600 years, almost 30 meters of sediment was accumulated and the turbidite activity was almost continuous. The average Pj values slightly decreased after 9.2 ka cal. BP in Unit 2 (1,016-1,222) associated to an abrupt shift in sedimentation rate. Despite this decrease, the sedimentation rate (0.02-0.18 cm/year) and the Pj values are still very high in comparison with hemipelagic sediments.

We propose that this increase in Pj is due to the exceptional sedimentation rate observed in core MD17&18, which can reach up to 9.5 cm/yr in Unit 1 causing an additional compaction effect, however, changes in particle size and mineralogy can play a secondary role.

Besides, magnetic mineralogy reveals that the magnetic minerals representative of the Ganges and Brahmaputra drainage area are magnetite, hematite and goethite. The Km record represents the fluctuations in the concentration of magnetite concentration and indicates higher supply of magnetite in Unit 1when the turbidite activity was the most important.

The difference in Km values between early and late Holocene suggest a modification of the sources of fluvial sediments within the Ganges-Brahmaputra catchment basin (highlands versus floodplain) related to changes in the intensity of the Asian summer monsoon. During early Holocene, stronger

monsoon yields a northwestward expansion of the area of precipitation in the Himalayas and the northern Indian subcontinent leading to a higher contribution of highlands sediments. Conversely, after 6 ka cal. BP, the detrital material mainly originated from the floodplain. These results are in agreement with previous work on core MD17&18 based on strontium and neodymium isotopic signatures (Joussain et al., 2017).

Our study shows that the use of AMS properties enables the identification of turbidite layers even when these are difficult to recognize using the classical technics based on grain-size and/or XRF analysis. Therefore, the AMS technique has a strong potential for the interpretation of changes in deposition regimes associated with climate or environmental changes.

Acknowledgements

This work was supported by the *Agence Nationale de la Recherche* project MONOPOL (grant ANR-11-BS56-0024). MONOPOL cruise aboard the Marion-Dufresne was supported by the IPEV, and the crew is acknowledged for its help. We are also grateful to MNHN and ISTeP technicians for their help during sampling and laboratory preparation: Lola Johannes, Ravi Dalliah and Florence Savignac. We are grateful for the comments and suggestions from two anonymous reviewers for suggestions and to improve the manuscript.

Figures

Figure 1: Location map from of cores MD12-3417 and MD12-3418CQ (composite core MD17&18) and core MD161/29 (Volvoikar et al. 2020) mentioned in this article. The map shows the physiography of the Ganges-Brahmaputra sedimentary system, from the catchment to the deep-sea fan (Fauquembergue et al. 2019). Fluvial systems are in light to dark blue (Curray et al., 2003; Kolla et al., 2012; Schwenk et al., 2003; Thomas et al., 2012; Thu et al., 2001; Weber et al., 2003). AV is the most recently active valley. The arrows indicate the surface current during southwest and northeast monsoon (Sun et al. 2019).

Figure 2 : From top to the bottom: the sedimentation rate and AMS ^{14}C ages; calcium carbonate contents (% $CaCO_3$) measured using a carbonate bomb and rock-eval measurements (white dots) and calibrated from XRF-Ca counts (line); ln(Ti/Ca) (inversed scale), ln (Zr/Rb) and ln(Si/Al) ratios measured by XRF; and d50 (mediam value in µm of the particle size distribution) estimated from laser granulometry. Age mode, XRF-Ti/Ca and Zr/Rb ratios and grain-size data were already published (Fournier et al., 2017) while the Si/Al ratio is published now for the first time. Depths are composite depths (cm) of core MD17&18. Recognized Units 1 and 2 are indicated on the top. Turbidite levels are indicated in green (Unit 1) and red (Unit 2).

Figure 3 : From top to the bottom: Percentage of silts+sands estimated from grain-size analysis (Fournier et al., 2017); IncI_3; corrected degree of anisotropy (Pj); foliation (F); lineation (L) and magnetic susceptibility measured on cubes. All theses parameters were obtained from the anisotropy of magnetic susceptibility measurements. Depths are composite depths (cm). Recognized Units 1 and 2 are indicated on the top. Turbidite levels are indicated in green (Unit 1) and red (Unit 2). The grey band indicates section XI of core MD12-3417 whose structure shows signs of disturbance associated with coring.

Figure 4 : From top to the bottom Flinn diagrams (L/F); a) Pj/T diagram; Pj-Km and Pj-d50 diagrams of core MD17&18. Data from the disturbed section 11 were not plotted. Turbites levels (T) were

differenciated from the "hemipelagic" sediment in each Unit using d50 and Zr/Rb records in Unit 1 and ln(Ti/Ca) record in Unit 2;

Figure 5: Stereoplots of principal axes orientations of the AMS ellipsoid in samples from Units 1 and 2. The plots are divided into two types, turbidites and hemipelagic sediments. Blue squares indicate K_1 axes (Kmax) and pink circles indicate K_3 axes (Kmin). The stereoplots are oriented to the the core generatrix and but not geographically oriented.

Figure 6: RT-SIRM ZFC/FC curves for three selected samples at 830 cm (Unit 2); 1627 cm (Unit 1) and 1733 cm (turbidite layer T1 from Unit 1). The arrows mark the cooling or warming direction for each curve.

Figure 7: Detailed results of the main AMS parameters presented in this study (Km, Pj, L et Inc K_3), the mean grain-size in µm (d50) and the R-X image obtained by scopix of one turbidite located in section 25 of core MD12-3417 between 3600 and 3670 cm (3665-3745 in composite depth).

Figure 8: Box charts displaying the mean, median and the first and third quartiles of Pj values from turbidites of Unit 1 (T1) and Unit 2 (T2) in the composite core MD17&18. Whiskers represent the standard deviation above and below the mean of the data (±1.5SD). Results were compared to the results from the distal portion of the Delgada deep-sea fan off northern California containing thin turbidite sand and silt layers (Joseph et al., 1998); samples of muddy levee sediments from Ursa Basin located on the northern Gulf of Mexico containing mass transport deposits (MTD) (Meissl et al., 2011) and samples of terrigenous sediments deposited in the South China Sea during the Pleistocene (Chen et al., 2017). In all cases, the samples depths are less than 50 meters.

Supplementary figures

Figure S1: X-ray diffraction analysis of selected samples from core MD12-3417 corresponding to unit 1, unit 2 and turbidites sequences. The main minerals identified were quartz, calcite, muscovite, clinochlore ferroan, amphibole (hornblende), feldspars (albite, sanidine) and clinopyroxene (diopside).

Figure S2: X-ray imagesof cores MD12-3418 and MD12-3417 performed using the Scopix X-ray imaging system (EPOC laboratory, University of Bordeaux). The first sections of core MD12-3417 shaded in red were not used in this sudy. Due to the high water and sand content in a turbidite, section XI of the MD12-3417 core shows signs of disturbance of the sedimentary structure

Figure S3: Evolution of the ARM/K ratio and the percentage of silts and sands as a function of depth between 700 and 2200 cm. The ARM/K is an indicator of magnetic grain size. Lower ARM/K ratio corresponds to higher magnetic grain-size. We observe a good correspondence between magnetic and sediment grain-size.

Table 1: Main AMS parameters of composite core MD17&18 used in the text (data will be provided if the manuscript is accepted).

References

Abdeldayem, A.L., 1999. Magnetic susceptibility anisotropy and remanence of some deep-sea sediments of the Tokai basin. In: Yuasa, M. (Ed.), Marine Geological Investigations of the Tokai Offhsore Area. Geological Survey. Japan Cruise Report 24, 127-146.

Abrajevitch, A., der Voo, R.V., Rea, D.K., 2009. Variations in relative abundances of goethite and hematite in Bengal Fan sediments. Climatic vs. diagenetic signals. Marine Geology 267, 191-206.

Banerjee, S. K., J. King and J. Marvin (1981). A rapid method for magnetic granulometry with applications to environmental studies. Geophysical research letters 8: 333-336.

Bassinot, F. , Beaufort L. (2012) MD 191 / MONOPOL cruise, RV Marion Dufresne, https://doi.org/10.17600/12200050

Baudin, F., Disnar, J.-R., Aboussou, A., Savignac, F., 2015. Guidelines for Rock–Eval analysis of recent marine sediments. Organic Geochemistry 86, 71-80.

Beckers, A., Beck, C., Hubert-Ferrari, A., Tripsanas, E., Crouzet, C., Sakellariou, D., Papatheodorou, G., De Batist, M., 2016. Influence of bottom currents on the sedimentary processes at the western tip of the Gulf of Corinth, Greece. Marine Geology 378, 312-332.

Boyle, J.F., Chiverrell, R.C., Schillereff, D.N., 2015. Approaches to Water Content Correction and Calibration for µXRF Core Scanning: Comparing X-ray Scattering with Simple Regression of Elemental Concentrations.

Bradák, B. and J. Kovács (2014). Quaternary surface processes indicated by the magnetic fabric of undisturbed, reworked and fine-layered loess in Hungary. Quaternary International 319: 76-87.

Calvert S.E., Price N.B. (1983) Geochemistry of Namibian Shelf Sediments. In: Suess E., Thiede J. (eds) Coastal Upwelling Its Sediment Record. NATO Conference Series (IV Marine Sciences), vol 10B. Springer, Boston, MA.

Campos, C., Beck, C., Crouzet, C., Carrillo, E., Van Welden, A., Tripsanas, E., 2014. Late Quaternary paleoseismic sedimentary archive from deep central Gulf of Corinth: time distribution of inferred earthquake-induced layers. Annals of Geophysics 56.

Campos, C., Beck, C., Crouzet, C., Demory, F., Van Welden, A., Eris, K., 2013. Deciphering hemipelagites from homogenites through anisotropy of magnetic susceptibility. Paleoseismic implications (Sea of Marmara and Gulf of Corinth). Sedimentary Geology 292, 1-14.

Carrillo, E., Beck, C., Audemard, F.A., Moreno, E., Ollarves, R., 2008. Disentangling Late Quaternary climatic and seismo-tectonic controls on Lake Mucubají sedimentation (Mérida Andes, Venezuela). Palaeogeography, Palaeoclimatology, Palaeoecology 259, 284-300.

Chen, Q., Kissel, C., Liu, Z., 2017. Late Quaternary climatic forcing on the terrigenous supply in the northern South China Sea: Input from magnetic studies. Earth and Planetary Science Letters 471, 160-171.

Curray, J.R., Emmel, F.J., Moore, D.G., 2003. The Bengal Fan: morphology, geometry, stratigraphy, history and processes. Marine and Petroleum Geology 19, 1191-1223.

Dypvik, H., Harris, N.B., 2001. Geochemical facies analysis of fine-grained siliciclastics using Th/U, Zr/Rb and (Zr+Rb)/Sr ratios. Chemical Geology 181, 131-146.

Ellwood, B. B. (1984). "Bioturbation; minimal effects on the magnetic fabric of some natural and experimental sediments." Earth and Planetary Science Letters 67: 367-367-376.

Fauquembergue, K., Fournier, L., Zaragosi, S., Bassinot, F., Kissel, C., Malaizé, B., Caley, T., Moreno, E., Bachelery, P., 2019. Factors controlling frequency of turbidites in the Bengal fan during the last 248 kyr cal BP: Clues from a presently inactive channel. Marine Geology 415, 105965.

Felletti, F., Dall'Olio, E., Muttoni, G., 2016. Determining flow directions in turbidites: An integrated sedimentological and magnetic fabric study of the Miocene Marnoso Arenacea Formation (northern Apennines, Italy). Sedimentary Geology 335, 197-215.

Fournier, L., K. Fauquembergue, S. Zaragosi, C. Zorzi, B. Malaizé, F. Bassinot, R. Joussain, C. Colin, E. Moreno and F. Leparmentier (2017). The Bengal fan: External controls on the Holocene Active Channel turbidite activity. The Holocene 27(6): 900-913.

Ge, S., Shi, X., Liu, Y., Wang, K., Zou, J., Diao, J., Zhu, Z., Wang, C., 2012. Turbidite and bottom-current evolution revealed by anisotropy of magnetic susceptibility of redox sediments in the Ulleung Basin, Sea of Japan. Chinese Science Bulletin 57, 660-672.

Goodbred, S.L.J., Kuehl, S.A., 2000. Enormous Ganges-Brahmaputra sediment discharge during strengthened early Holocene monsoon. Geology 28, 1083.

Gupta, A.K., Das, M., Anderson, D.M., 2005. Solar influence on the Indian summer monsoon during the Holocene. Geophysical Research Letters 32. L17703_1-L17703_4.

Joseph, L.H., Rea, D.K., Pluijm, B.A.v.d., 1998. Use of grain size and magnetic fabric analyses to distinguish among depositional environments. Paleoceanography 13, 491-501.

Joussain, R., Liu, Z., Colin, C., Duchamp-Alphonse, S., Yu, Z., Moréno, E., Fournier, L., Zaragosi, S., Dapoigny, A., Meynadier, L., Bassinot, F., 2017. Link between Indian monsoon rainfall and physical erosion in the Himalayan system during the Holocene. Geochemistry, Geophysics, Geosystems 18, 3452-3469.

Kawamura, K., Ogawa, Y., 2004. Progressive change of pelagic clay microstructure during burial process: examples from piston cores and ODP cores. Marine Geology 207, 131-144.

King, J. W., S. K. Banarjee, J. Marvin and O. Ozdemir (1982). A comparison of different magnetic methods for determinating the relative grain-size of magnetite in natural materials: Some results from lake sediments. Earth and Planetary science letters 59: 404-419.

Kissel, C., Laj, C., Lehman, B., Labyrie, L., Bout-Roumazeilles, V., 1997. Changes in the strength of the Iceland-Scotland Overflow Water in the last 200,000 years: Evidence from magnetic anisotropy analysis of core SU90-33. Earth and Planetary Science Letters 152, 25-36.

Kissel, C., Laj, C., Mazaud, A., Dokken, T., 1998. Magnetic anisotropy and environmental changes in two sedimentary cores from the Norwegian Sea and the North Atlantic. Earth and Planetary Science Letters 164, 617-626.

Kolla, V., Bandyopadhyay, A., Gupta, P., Mukherjee, B., Ramana, D.V., 2012. Morphology and Internal Structure of a Recent Upper Bengal Fan-Valley Complex, in: Prather, B.E., Deptuck, M.E., Mohrig, D., Hoorn, B.V., Wynn, R.B. (Eds.), Application of the Principles of Seismic Geomorphology to Continental Slope and Base-of-Slope Systems: Case Studies from SeaFloor and Near-Sea Floor Analogues. SEPM Society for Sedimentary Geology, p. 0.

Kuhnt, W., Holbourn, A., Xu, J., Opdyke, B., Deckker, P., Röhl, U., Mudelsee, W., 2015. Southern hemisphere control on Australian monsoon variability during the late deglaciation and Holocene. Nature Comm 6, 5916.

Kumar, K., Agrawal, S., Sharma, A., Pandey, S., 2019. Indian summer monsoon variability and vegetation changes in the core monsoon zone, India, during the Holocene: A multiproxy study. The Holocene 29, 110-119.

Lambeck, K., Rouby, H., Purcell, A., Sun, Y., Sambridge, M., 2014. Sea level and global ice volumes from the Last Glacial Maximum to the Holocene. Proceedings of the National Academy of Sciences 111, 15296-15303.

Liu, X., Rendle-Bühring, R., Henrich, R., 2018. High-and low-latitude forcing of the East African climate since the LGM: Inferred from the elemental composition of marine sediments off Tanzania. Quaternary Science Reviews 196, 124-136.

Liu, J., He, W., Cao, L., Zhu, Z., Xiang, R., Li, T., Shi, X., Liu, S., 2019. Staged fine-grained sediment supply from the Himalayas to the Bengal Fan in response to climate change over the past 50,000 years. Quaternary Science Reviews 212, 164-177.

Liu, X., Fike, D., Li, A., Dong, L., Xu, F., Zhuang, G., Rendle-Bühring, R., Wan, S., 2019. Pyrite sulfur isotopes constrained by sedimentation rates: Evidence from sediments on the East China Sea inner shelf since the late Pleistocene. Chemical Geology 505, 66-75.

Lupker, M., France-Lanord, C., Galy, V., Lavé, J., Kudrass, H., 2013. Increasing chemical weathering in the Himalayan system since the Last Glacial Maximum. Earth and Planetary Science Letters 365, 243-252.

Maffione, M., Morris, A., 2017. The onset of fabric development in deep marine sediments. Earth and Planetary Science Letters 474, 32-39.Martín-Hernández, F., Hirt, A.M., 2003. The anisotropy of magnetic susceptibility in biotite, muscovite and chlorite single crystals. Tectonophysics 367, 13-28.

Meissl, S., Behrmann, J.H., Franke, C., 2011. Magnetic fabrics in Quaternary sediments, Ursa Basin, northern Gulf of Mexico record transport processes, compaction and submarine slumping. Marine Geology 286, 51-64.

Migeon, S., Weber, O., Faugeres, J.C., Saint-Paul, J., 1998. SCOPIX: A new X-ray imaging system for core analysis. Geo-Marine Letters 18, 251-255.

Milliman, J.D., 2001. River inputs, in: J. H. Steele, K. K. Turekian, Thorpe, S.A. (Eds.), Encyclopedia of Ocean Sciences. Elsevier, pp. 2419-2427.

Moreno, E., Marty, G., Fournier, L., Zaragosi, S., Fauquembergue, K., Bassinot, F., Garidel-Thoron, T., Valet, J.-P., 2014. Magnetic properties of marine sediments from the Bengal Fan: record of climatic changes during Holocene and turbiditic activity from the river system, Castle meeting: New trends on Paleo, Rock and Environmental Magnetism, Evora (Portugal).

Mulder, T., Zaragosi, S., Razin, P., Grelaud, C., Lanfumey, V., Bavoil, F., 2009. A new conceptual model for the deposition process of homogenite: Application to a cretaceous megaturbidite of the western Pyrenees (Basque region, SW France). Sedimentary Geology 222, 263-273.

Özdemir, Ö., Dunlop, D.J., 2010. Hallmarks of maghemitization in low-temperature remanence cycling of partially oxidized magnetite nanoparticles. Journal of Geophysical Research: Solid Earth 115, 148-227.

Özdemir, Ö., Dunlop, D.J., Berquó, T.S., 2008. Morin transition in hematite: Size dependence and thermal hysteresis. Geochemistry, Geophysics, Geosystems 9.

Parés, J.M., Hassold, N.J.C., Rea, D.K., van der Pluijm, B.A., 2007. Paleocurrent directions from paleomagnetic reorientation of magnetic fabrics in deep-sea sediments at the Antarctic Peninsula Pacific margin (ODP Sites 1095, 1101). Marine Geology 242, 261-269.

Park, M.E., Cho, H., Son, M., Sohn, Y.K., 2013. Depositional processes, paleoflow patterns, and evolution of a Miocene gravelly fan-delta system in SE Korea constrained by anisotropy of magnetic susceptibility analysis of interbedded mudrocks. Marine and Petroleum Geology 48, 206-223.

Phillips, S.C., Johnson, J.E., Clyde, W.C., Setera, J.B., Maxbauer, D.P., Severmann, S., Riedinger, N., 2017. Rock magnetic and geochemical evidence for authigenic magnetite formation via iron reduction in coal-bearing sediments offshore Shimokita Peninsula, Japan (IODP Site C0020). Geochemistry, Geophysics, Geosystems 18, 2076-2098.

Revel, M., Ducassou, E., Skonieczny, C., Colin, C., Bastian, L., Bosch, D., Migeon, S., Mascle, J., 2015. 20,000 years of Nile River dynamics and environmental changes in the Nile catchment area as inferred from Nile upper continental slope sediments. Quaternary Science Reviews 130, 200-221.

Schwehr, K., Tauxe, L., Driscoll, N., Lee, H., 2006. Detecting compaction disequilibrium with anisotropy of magnetic susceptibility. Geochemistry, Geophysics, Geosystems 7.

Schwenk, T., Spieß, V., Hübscher, C., Breitzke, M., 2003. Frequent channel avulsions within the active channel–levee system of the middle Bengal Fan—an exceptional channel–levee development derived from Parasound and Hydrosweep data. Deep Sea Research Part II: Topical Studies in Oceanography 50, 1023-1045.

Sharma, S., Joachimski, M., Sharma, M., Tobschall, H.J., Singh, I.B., Sharma, C., Chauhan, M.S., Morgenroth, G., 2004. Lateglacial and Holocene environmental changes in Ganga plain, Northern India. Quaternary Science Reviews 23, 145-159.

St-Onge, G., Mulder, T., Francus, P., Long, B., 2007. Chapter Two Continuous Physical Properties of Cored Marine Sediments, in: Hillaire–Marcel, C., De Vernal, A. (Eds.), Developments in Marine Geology. Elsevier, pp. 63-98.

Suganuma, Y., Yamazaki, T., Kanamatsu, T., 2009. South Asian monsoon variability during the past 800 kyr revealed by rock magnetic proxies. Quaternary Science Reviews 28, 926-938.

Sun, X., Liu, S., Li, J., Zhang, H., Zhu, A., Cao, P., Chen, M.-T., Zhao, G., Khokiattiwong, S., Kornkanitnan, N., Shi, X., 2019. Major and trace element compositions of surface sediments from the lower Bengal Fan: Implications for provenance discrimination and sedimentary environment. Journal of Asian Earth Sciences 184, 104000.

Taira, A., 1989. Magnetic fabrics and depositional processes, Sedimentary Facies in the Active Plate Margin,. Terra Scientific Publishing Company, Tokyo, Japan, pp. 43-77.

Tamaki, M., Suzuki, K., Fujii, T., 2015. Paleocurrent analysis of Pleistocene turbidite sediments in the forearc basin inferred from anisotropy of magnetic susceptibility and paleomagnetic data at the gas hydrate production test site in the eastern Nankai Trough. Marine and Petroleum Geology 66, 404-417.

Tjallingii, R., Röhl, U., Kölling, M., Bickert, T., 2007. Influence of the water content on X-ray fluorescence core-scanning measurements in soft marine sediments. Geochemistry, Geophysics, Geosystems 8.

Tanty, C., Valet, J.-P., Carlut, J., Bassinot, F., Zaragosi, S., 2016. Acquisition of detrital magnetization in four turbidites. Geochemistry, Geophysics, Geosystems 17, 3207-3223.

Tarling, D.H., Hrouda, F., 1993. The magnetic Anisotropy of Rocks, 1 ed. Chapman &Hall.

Taylor, S.N., Lagroix, F., Rousseau, D., Antoine, P., 2014. Mineral magnetic characterization of the Upper Pleniglacial Nussloch loess sequence (Germany): an insight into local environmental processes. Geophysical Journal International 199, 1463-1480.

Thamban, M., Kawahata, H., Rao, V.P., 2007. Indian summer monsoon variability during the Holocene as recorded in sediments of the Arabian Sea: Timing and implications. Journal of Oceanography 63, 1009-1020.

Thomas, B.L., Cutler, M., Novak, C., 2012. A modified counterconditioning procedure prevents the renewal of conditioned fear in rats. Learning and Motivation 43, 24-34.

Thu, M.K., Tokuyama, H., Murayama, M., party, K.H.s., 2001. HINDOO cruise deep-sea channel survey in the Bay of Bengal. 地質学雑誌 107, XIX-XX.

Unger, D., Ittekkot, V., Schäfer, P., Tiemann, J., Reschke, S., 2003. Seasonality and interannual variability of particle fluxes to the deep Bay of Bengal: influence of riverine input and oceanographic processes. Deep Sea Research Part II: Topical Studies in Oceanography 50, 897-923.

Volvoikar, S., Mazumdar, A., Peketi, A., Dewangan, P., Sawant, B., Manaskanya, A., Goswami, H., Das, D., Pujari, S., 2020. Contrasting sulfidization in the turbidite and hemipelagic sediments of Bengal Fan. Marine and Petroleum Geology 118, 104408.

Weber, M.E., Wiedicke-Hombach, M., Kudrass, H.R., Erlenkeuser, H., 2003. Bengal Fan sediment transport activity and response to climate forcing inferred from sediment physical properties. Sedimentary Geology 155, 361-381.

Weber, M.E., Wiedicke, M.H., Kudrass, H.R., Hübscher, C., Erlenkeuser, H., 1997. Active growth of the Bengal Fan during sea-level rise and highstand. Geology 25, 315-318.

Weltje, G.J., Tjallingii, R., 2008. Calibration of XRF core scanners for quantitative geochemical logging of sediment cores: Theory and application. Earth and Planetary Science Letters 274, 423.

Zhang, Y.G., Ji, J., Balsam, W.L., Liu, L., Chen, J., 2007. High resolution hematite and goethite records from ODP 1143, South China Sea: Co-evolution of monsoonal precipitation and El Niño over the past 600,000 years. Earth and Planetary Science Letters 264, 136-150.

Core name	Unit	Composite depth (cm)	Km (10^{-6} SI)	F	L	Pj	T	K_1 dec	K_1 inc	K_2 dec	K_2 inc	K_3 dec	K_3 inc
MD12-3418CQ	Unit 2	4	261,65	1,006	1,022	1,03	-0,561	223,6	9,8	326,2	51,6	126,2	36,7
MD12-3418CQ	Unit 2	39	292,26	1,008	1,008	1,016	0,061	227,9	34,1	325,3	10,7	70,3	53,8
MD12-3418CQ	Unit 2	72	288,41	1,113	1,004	1,135	0,934	24,2	2	114,3	1	230,2	87,8
MD12-3418CQ	Unit 2	75	286,45	1,117	1,004	1,14	0,923	201,1	0	291,1	1	108,5	89
MD12-3418CQ	Unit 2	87	312,55	1,119	1,012	1,147	0,808	29,5	0,5	119,5	0,5	252,9	89,3
MD12-3418CQ	Unit 2	96,5	282,79	1,023	1,03	1,054	-0,133	169,6	31,9	260,7	1,8	353,6	58
MD12-3418CQ	Unit 2	111,5	262,52	1,087	1,005	1,104	0,888	214	2,7	304	1	53,9	87,1
MD12-3418CQ	Unit 2	122,5	230,72	1,127	1,004	1,151	0,934	131,3	0,2	61,2	3	245,3	87
MD12-3418CQ	Unit 2	126,5	273,22	1,113	1,002	1,133	0,962	137,1	2,8	46,8	5,2	255,2	84,1
MD12-3418CQ	Unit 2	132,5	311,21	1,112	1,008	1,126	0,865	355,5	2,7	85,6	2,4	217,5	86,4
MD12-3418CQ	Unit 2	136,5	324,15	1,133	1,003	1,157	0,956	332,8	2,2	62,9	3,5	211	85,8
MD12-3418CQ	Unit 2	142,5	282,11	1,04	1,012	1,165	0,828	16,7	17,6	106,9	0,7	199	72,4
MD12-3418CQ	Unit 2	149,5	376,01	1,11	1,006	1,179	0,919	3	10,4	272,7	1,9	172,5	79,4
MD12-3418CQ	Unit 2	150,5	323,71	1,054	1,015	1,074	0,565	42,2	4	311,8	5,3	169,2	83,4
MD12-3418CQ	Unit 2	156,5	296,44	1,04	1,006	1,05	0,734	74,4	11,4	344,1	1,5	246,6	78,5
MD12-3418CQ	Unit 2	162,5	313,24	1,01	1,018	1,029	-0,281	42,1	7,3	306,1	39,3	140,9	49,7
MD12-3418CQ	Unit 2	171,5	299,51	1,073	1,003	1,087	0,905	341,5	2,2	161,7	4	156,15	85,4
MD12-3418CQ	Unit 2	174,5	315,12	1,029	1,002	1,035	0,86	99,4	3,4	9	6,6	216,1	82,6
MD12-3418CQ	Unit 2	177,5	319,92	1,018	1,011	1,03	0,239	74,9	13,7	343,4	6	230,1	75
MD12-3418CQ	Unit 2	184,5	311,08	1,03	1,017	1,048	0,255	3,6	7,6	271	19,3	114,1	69,1
MD12-3418CQ	Unit 2	192,5	316,8	1,048	1,008	1,061	0,714	144,4	5,3	52,3	21,7	247,4	67,6
MD12-3418CQ	Unit 2	197,5	303,88	1,024	1,009	1,034	0,469	75,6	11,3	167,1	7,2	288,9	76,6
MD12-3418CQ	Unit 2	201,5	308,66	1,117	1,002	1,138	0,965	325	1,7	55,2	5	215,9	84,7
MD12-3418CQ	Unit 2	210,5	323,83	1,047	1,007	1,059	0,743	79,5	14,3	348,7	3,2	246,4	75,3
MD12-3418CQ	Unit 2	216,5	268,81	1,085	1,004	1,101	0,9	35,9	7,3	126,2	2,6	235,5	82,3
MD12-3418CQ	Unit 2	217,5	336,31	1,016	1,018	1,034	-0,072	80,6	28	177	11,9	287,6	59,2
MD12-3418CQ	Unit 2	221,5	319,68	1,013	1,023	1,037	-0,26	352	12,2	257	22,3	108,6	64,3
MD12-3418CQ	Unit 2	229,5	252,98	1,057	1,006	1,069	0,808	256,8	5,8	346,9	0,3	79,4	84,2

Core name	Unit	Composite depth (cm)	Km (10^{-6} SI)	F	L	Pj	T	K_1 dec	K_1 inc	K_2 dec	K_2 inc	K_3 dec	K_3 inc
MD12-3418CQ	Unit 2	235,5	307,07	1,033	1,01	1,045	0,532	109,5	16,1	16	12	251	69,7
MD12-3418CQ	Unit 2	241,5	338,14	1,021	1,008	1,031	0,433	299	9,1	32,9	22,7	188,6	65,3
MD12-3418CQ	Unit 2	250,5	317,33	1,04	1,01	1,054	0,58	87,8	18,4	179	3,5	279,5	71,2
MD12-3418CQ	Unit 2	259,5	307,83	1,047	1,005	1,058	0,798	96,6	3	5,8	15,8	197	73,9
MD12-3418CQ	Unit 2	261,5	293,92	1,031	1,002	1,037	0,86	184	12,5	274,6	2,7	16,5	77,3
MD12-3418CQ	Unit 2	270,5	279,52	1,072	1,013	1,093	0,675	202,6	2,5	112	13,1	303,3	76,6
MD12-3418CQ	Unit 2	281,5	247,86	1,067	1,016	1,089	0,617	40,2	4,8	310	2,7	190,5	84,4
MD12-3418CQ	Unit 2	292,5	274,69	1,069	1,003	1,082	0,91	145,8	3	55,5	4,2	271,5	84,8
MD12-3418CQ	Unit 2	306,5	350,47	1,045	1,018	1,065	0,428	57,2	5,7	326,7	5,8	191,4	81,9
MD12-3418CQ	Unit 2	312,5	260,27	1,064	1,017	1,037	0,569	76,9	8,4	167,1	1,6	268	81,5
MD12-3418CQ	Unit 2	328,5	265,8	1,033	1,03	1,064	0,051	328	3,3	58,5	8	215,8	81,3
MD12-3418CQ	Unit 2	333,5	260,61	1,142	1,094	1,168	0,947	32,3	1,2	122,4	3,2	281,3	86,6
MD12-3418CQ	Unit 2	342	298,92	1,051	1,005	1,063	0,804	48,2	10,3	138,4	0,9	233,1	79,7
MD12-3418CQ	Unit 2	347,5	265,42	1,056	1,017	1,078	0,518	51,9	1,6	142	4,1	300,3	85,6
MD12-3418CQ	Unit 2	352,5	279,87	1,094	1,012	1,117	0,772	63,3	9,6	153,4	0,2	244,5	80,4
MD12-3418CQ	Unit 2	361,5	271,52	1,156	1,006	1,187	0,92	24,4	5,6	294,3	1,8	186,7	84,1
MD12-3418CQ	Unit 2	368,5	262,74	1,038	1,005	1,047	0,747	41	6,1	310,9	1,3	209	83,8
MD12-3418CQ	Unit 2	376	310,29	1,038	1,024	1,064	0,215	353,6	0,6	83,8	18,6	261,8	71,4
MD12-3418CQ	Unit 2	381,5	282,83	1,028	1,005	1,036	0,671	233,9	2,7	143,6	6,5	346,2	83
MD12-3418CQ	Unit 2	387,5	280,78	1,05	1,017	1,071	0,488	108,8	1,4	18,4	15,1	204	74,8
MD12-3418CQ	Unit 2	391,5	333,35	1,062	1,016	1,084	0,576	43,9	2,8	312,8	20,7	141,1	69,1
MD12-3418CQ	Unit 2	401	225,48	1,059	1,013	1,078	0,623	80,6	0,3	350,6	1,8	181,6	88,2
MD12-3418CQ	Unit 2	411	267,06	1,037	1,014	1,054	0,448	32,8	4,4	123,7	11,5	282	77,7
MD12-3418CQ	Unit 2	417	275,17	1,084	1,01	1,105	0,782	307,8	0,7	37,9	2	198,1	87,9
MD12-3418CQ	Unit 2	426,5	268,03	1,109	1,012	1,135	0,794	284,1	1,3	14,2	4,8	178,9	85
MD12-3418CQ	Unit 2	433	276,88	1,121	1,005	1,145	0,917	58,7	4,3	148,9	3,6	278,9	84,4
MD12-3418CQ	Unit 2	441	283,71	1,151	1,011	1,184	0,86	288,8	0,3	18,8	1,4	185,8	88,5
MD12-3418CQ	Unit 2	447	282,62	1,136	1,003	1,161	0,953	47,4	3,2	137,5	2	259,3	86,2

Core name	Unit	Composite depth (cm)	Km (10^{-6} SI)	F	L	Pj	T	K_1 dec	K_1 inc	K_2 dec	K_2 inc	K_3 dec	K_3 inc
MD12-3418CQ	Unit 2	456,5	306,16	1,163	1,002	1,192	0,969	47,3	0,8	317,2	5,8	144,7	84,2
MD12-3418CQ	Unit 2	463	275,5	1,027	1,008	1,037	0,517	225	2,6	315,1	0,8	62,6	87,3
MD12-3418CQ	Unit 2	470	279,2	1,065	1,01	1,082	0,732	47,3	2,7	317,3	0,8	210,4	87,2
MD12-3418CQ	Unit 2	479	257,44	1,034	1,028	1,063	0,102	66	2,8	156,4	8,2	317,3	81,4
MD12-3418CQ	Unit 2	481	223,52	1,109	1,002	1,129	0,954	149,5	5,4	59,2	2,9	300,8	83,9
MD12-3418CQ	Unit 2	488	269,35	1,131	1,004	1,155	0,945	19	5,1	288,8	2,2	175,7	84,4
MD12-3418CQ	Unit 2	493	287,65	1,131	1,001	1,153	0,982	152,6	3,8	62,4	2,4	300	85,5
MD12-3418CQ	Unit 2	502,5	279,46	1,126	1,001	1,148	0,982	30,1	1,5	299,9	5,9	133,9	83,9
MD12-3418CQ	Unit 2	510	293,24	1,133	1,001	1,156	0,977	46,8	0,9	136,8	1	274,9	88,6
MD12-3418CQ	Unit 2	519,5	261,82	1,044	1,004	1,053	0,923	1,5	8,6	91,7	0,9	187,9	81,3
MD12-3418CQ	Unit 2	527	302,74	1,061	1,006	1,075	0,822	44,7	3,7	313,9	12,9	150,5	76,6
MD12-3418CQ	Unit 2	535,5	269,45	1,156	1,005	1,193	0,818	95,1	0,7	5	4,5	194,3	85,5
MD12-3418CQ	Unit 2	541	291,53	1,041	1,005	1,053	0,793	60,5	7,1	150,7	1,9	255,5	82,7
MD12-3418CQ	Unit 2	551	313,15	1,047	1,022	1,072	0,349	218,2	2,2	128,1	2,7	346,7	86,5
MD12-3418CQ	Unit 2	557	264,46	1,157	1,004	1,162	0,939	30,8	2,7	300,8	0,2	207,5	87,3
MD12-3418CQ	Unit 2	561	281,83	1,136	1,011	1,167	0,846	43,2	1,2	133,3	6,3	303	83,6
MD12-3418CQ	Unit 2	566	277,29	1,141	1,018	1,177	0,766	30,3	4,2	300	4,3	164,3	83,9
MD12-3418CQ	Unit 2	570	259,88	1,136	1,008	1,163	0,886	36,4	1,3	126,5	4,7	291,2	85,1
MD12-3418CQ	Unit 2	577	232,95	1,025	1,01	1,035	0,438	30,4	3,3	300,1	5,5	151,5	83,6
MD12-3418CQ	Unit 2	583	202,67	1,048	1,012	1,064	0,596	222,2	0,1	312,2	3,8	130,6	86,2
MD12-3418CQ	Unit 2	588	229,58	1,049	1,011	1,064	0,64	40	7,8	309,6	3,3	196,9	81,5
MD12-3418CQ	Unit 2	594	195,44	1,032	1,007	1,042	0,647	234,5	4,4	325,4	12,3	125,2	77
MD12-3418CQ	Unit 2	599	210,79	1,039	1,002	1,047	0,898	55,6	5,2	325,5	1,3	221,1	84,6
MD12-3418CQ	Unit 2	607	214,69	1,056	1,012	1,074	0,634	220,3	0,5	130,3	2,9	319,4	87
MD12-3418CQ	Unit 2	615	234,61	1,123	1,004	1,146	0,931	39,7	1,2	129,8	3,5	291	86,3
MD12-3418CQ	Unit 2	624	147,25	1,155	1,005	1,179	0,927	6,1	5,6	96,2	0,7	192,9	84,4
MD12-3418CQ	Unit 2	640,5	217,41	1,111	1,009	1,135	0,848	358,1	4,4	268	0,1	176,5	85,6
MD12-3418CQ	Unit 2	647	243,47	1,095	1,004	1,113	0,918	37,7	0,6	127,8	6,8	302,8	83,1

Core name	Unit	Composite depth (cm)	Km (10^{-6} SI)	F	L	Pj	T	K_1 dec	K_1 inc	K_2 dec	K_2 inc	K_3 dec	K_3 inc
MD12-3418CQ	Unit 2	653,5	251,63	1,131	1,008	1,159	0,882	355,6	6	85,6	0,2	177,1	84
MD12-3418CQ	Unit 2	657	225,45	1,173	1,01	1,209	0,887	215,2	1,7	125	5,2	323,5	84,5
MD12-3418CQ	Unit 2	665	197,88	1,071	1,007	1,087	0,811	99,7	7,7	8,7	7,5	234,9	79,2
MD12-3418CQ	Unit 2	670	228,42	1,058	1,009	1,074	0,717	212,3	1	121,9	16,8	305,7	73,2
MD12-3418CQ	Unit 2	677,5	158,2	1,183	1,01	1,222	0,89	348,7	5,7	78,7	0,5	173,7	84,3
MD12-3418CQ	Unit 2	682	221,46	1,108	1	1,125	0,99	107,5	5,4	17,4	1,1	276,2	84,5
MD12-3418CQ	Unit 2	688,5	198,25	1,039	1,014	1,055	0,465	27,2	2,7	306,9	7	148,2	82,5
MD12-3418CQ	Unit 2	694	232,56	1,061	1,011	1,077	0,692	132	1,1	41,9	4	237,8	85,9
MD12-3418CQ	Unit 2	701	228,38	1,039	1,011	1,053	0,562	134,9	2,9	44,4	9,8	241,3	79,8
MD12-3418CQ	Unit 2	708	207,82	1,039	1,01	1,051	0,699	77,1	6,3	346,5	5,5	215,7	81,7
MD12-3418CQ	Unit 2	718	231,43	1,039	1,012	1,054	0,512	115,3	2	205,4	2	340,5	87,2
MD12-3418CQ	Unit 2	725	242,09	1,066	1,01	1,083	0,722	217,5	4,4	307,8	3,5	76,3	84,4
MD12-3418CQ	Unit 2	734,5	226,14	1,044	1,01	1,056	0,601	55	8,2	325	0,1	234,2	81,8
MD12-3418CQ	Unit 2	741	242,74	1,059	1,006	1,073	0,811 5	54,35	4,05	144,6	4,4	281,45	83,9
MD12-3418CQ	Unit 2	751	243,01	1,057	1,011	1,074	0,657	45,8	7,1	315,2	5	190,6	81,3
MD12-3418CQ	Unit 2	757	224,2	1,149	1,006	1,178	0,921	22,2	6,1	291,7	4,1	168,4	82,6
MD12-3418CQ	Unit 2	761,5	207,15	1,041	1,004	1,05	0,827	71,3	1,9	341,1	6,4	177,5	83,4
MD12-3418CQ	Unit 2	767,5	221,34	1,083	1,001	1,097	0,972	280,4	7,2	12,6	16,86	167,8	71,8
MD12-3418CQ	Unit 2	771,5	233,34	1,052	1,015	1,072	0,545	0,5	5,6	91,7	12,44	246,6	76,4
MD12-3417	Unit 2	772,2	231,57	1,067	1,008	1,083	0,776	332,2	5,4	64,1	19,32	227,2	70
MD12-3417	Unit 2	783,7	227,27	1,046	1,006	1,057	0,77	115,5	9,3	206,3	4,9	323,6	79,5
MD12-3417	Unit 2	807,4	222,98	1,053	1,021	1,078	0,423	60,7	2,4	151,1	9,4	316,6	80,3
MD12-3417	Unit 2	831,1	222,14	1,119	1,001	1,139	0,98	196,3	2	106	6,6	302,7	83,1
MD12-3417	Unit 2	854,8	212,39	1,048	1,01	1,063	0,648	97	6,7	6,3	5,6	236,4	81,2
MD12-3417	Unit 2	870,8	228,83	1,137	1,004	1,163	0,944	63,2	1,7	153,3	4,9	313,8	84,8
MD12-3417	Unit 2	890,9	195,51	1,061	1,013	1,078	0,64	140,3	7,2	231,3	8,5	10,5	78,8
MD12-3417	Unit 2	914,6	216,4	1,147	1,006	1,176	0,911	6,3	4,6	96,7	6,11	239,1	82,4
MD12-3417	Unit 2	938,3	243,37	1,031	1,012	1,044	0,443	142,6	4,8	51,6	3,25	255,3	77,7
MD12-3417	Unit 2	962	258,67	1,13	1,012	1,166	0,833	109,4	5,8	18,9	4,6	251,1	82,6

Core name	Unit	Composite depth (cm)	Km (10^{-6} SI)	F	L	Pj	T	K_1 dec	K_1 inc	K_2 dec	K_2 inc	K_3 dec	K_3 inc
MD12-3417	Unit 2	985,6	270,56	1,046	1,002	1,058	0,927	170,7	6,2	80,1	5,6	308,5	81,7
MD12-3417	Unit 2	1031,2	251,87	1,028	1,01	1,04	0,448	83,5	8,2	174,4	6,1	300,8	79,7
MD12-3417	Unit 2	1039,5	292,49	1,026	1,038	1,065	-0,188	68,1	17,8	334,9	10	216,9	69,4
MD12-3417	Unit 2	1051,4	327,51	1,029	1,018	1,048	0,224	98,5	21,3	3,6	12,3	245,7	65,1
MD12-3417	Unit 2	1063,2	327,82	1,079	1,017	1,104	0,646	94,9	14,7	1,6	12,4	233	70,6
MD12-3417	Unit 1	1098,7	381,88	1,016	1,012	1,028	0,124	103,9	8,3	16,5	3,2	265,7	81,1
MD12-3417	Unit 1	1122,4	328,38	1,071	1,006	1,087	0,835	88,3	14,2	356,6	6,8	241,8	74,2
MD12-3417	Unit 1	1146,1	400,77	1,056	1,009	1,071	0,711	98,3	10,7	6,7	8,1	240,4	76,5
MD12-3417	Unit 1	1169,8	250,02	1,077	1,007	1,085	0,821	115,6	10,7	23,4	11,5	247,4	74,2
MD12-3417	Disturbed	1181,6	208,7	1,079	1,018	1,104	0,623	349,9	50,8	113,6	24,3	217,8	28,6
MD12-3417	Disturbed	1188,7	295,95	1,086	1,021	1,115	0,605	110,9	58,3	232,4	17,9	331,1	25,2
MD12-3417	Disturbed	1200,6	245,67	1,09	1,016	1,117	0,685	355,3	35,4	111,8	32	231,3	38,2
MD12-3417	Disturbed	1207,7	368,49	1,028	1,046	1,076	-0,245	33,7	51,3	155,2	22,8	258,9	29,4
MD12-3417	Disturbed	1212,4	219,13	1,09	1,003	1,107	0,935	192	51,1	75,7	19,7	332,8	32
MD12-3417	Disturbed	1218,3	217,8	1,062	1,019	1,087	0,521	348,1	40,4	118,2	37,1	231,6	27,7
MD12-3417	Disturbed	1224,2	264,28	1,081	1,022	1,111	0,562	1,8	48,6	125	25,7	231,1	29,9
MD12-3417	Disturbed	1229	278,28	1,085	1,022	1,115	0,584	11,6	51,3	135,1	23,9	239	28,5
MD12-3417	Disturbed	1247,9	197,31	1,071	1,014	1,092	0,662	111,2	64,9	236,1	15	331,5	19,7
MD12-3417	Disturbed	1271,6	530,35	1,021	1,022	1,041	-0,049	4,1	21,5	97,9	9,6	210,4	66,3
MD12-3417	Disturbed	1277,5	445,2	1,061	1,012	1,079	0,659	305,1	2,6	35,3	4,1	182,7	85,2
MD12-3417	Disturbed	1283,5	384,35	1,058	1,021	1,084	0,458	113,7	85,4	263	4	353,2	2,3
MD12-3417	Disturbed	1289,4	242,16	1,064	1,007	1,079	0,797	95,3	28	337	41,7	207,6	35,5
MD12-3417	Disturbed	1295,3	276,43	1,051	1,008	1,063	0,719	338,6	72,4	93,1	7,5	185,2	15,8
MD12-3417	Disturbed	1301,2	315,71	1,028	1,052	1,083	-0,293	262,5	3,2	352,5	0,4	89	86,8
MD12-3417	Disturbed	1307,1	253,29	1,065	1,022	1,092	0,483	357,1	13,9	98	37,3	250,5	49,3
MD12-3417	Disturbed	1313,1	264,92	1,082	1,024	1,111	0,532	355,1	13,2	97,8	43,1	252	43,9
MD12-3417	Disturbed	1319	279,67	1,072	1,022	1,1	0,528	83,5	11,1	181,6	35,8	339,1	52
MD12-3417	Disturb	1324,9	226,46	1,06	1,018	1,091	0,56	5,6	8,4	99,8	26,	259,4	62,2

Core name	Unit	Composite depth (cm)	Km (10^{-6} SI)	F	L	Pj	T	K_1 dec	K_1 inc	K_2 dec	K_2 inc	K_3 dec	K_3 inc
MD12-3417	Disturbed	1332	260,04	1,067	1,018	1,09	0,572	347,1	4,4	79,5	28,7	249,2	60,9
MD12-3417	Disturbed	1339,1	278,33	1,08	1,022	1,109	0,565	353,5	4,8	86,5	31,8	255,8	57,8
MD12-3417	Disturbed	1342,7	342,31	1,058	1,036	1,096	0,227	83,8	10,2	182,2	39,1	341,8	49,1
MD12-3417	Disturbed	1351	354,36	1,084	1,04	1,129	0,347	359	14,5	90,8	6,8	205,4	73,9
MD12-3417	Unit 1	1359,8	255,65	1,085	1,044	1,135	0,306	127,1	2,4	217,4	5,7	14,1	83,8
MD12-3417	Unit 1	1361	249,71	1,142	1,002	1,167	0,972	3[illegible]1	3	229	2,5	99,3	86,1
MD12-3417	Unit 1	1363,4	230,28	1,12	1,002	1,141	0,973	321,8	2,3	231,7	2,3	97	86,7
MD12-3417	Unit 1	1369,3	248,35	1,13	1,001	1,153	0,976	353,5	4	263,4	1,1	157,6	85,8
MD12-3417	Unit 1	1380	271,37	1,085	1,014	1,103	0,694	176,2	0,1	186,2	1,3	8,9	88,7
MD12-3417	Unit 1	1382,3	214,22	1,119	1,005	1,142	0,922	338,8	0,3	68,8	0,1	179,5	89,7
MD12-3417	Unit 1	1389,4	228,23	1,123	1,009	1,15	0,855	338,4	0,8	248,3	4,9	77,9	85,1
MD12-3417	Unit 1	1397,7	260,33	1,153	1,011	1,157	0,854	331,2	5	240,8	5,4	103,9	82,7
MD12-3417	Unit 1	1403,6	343,87	1,106	1,017	1,135	0,717	117,2	2	207,2	1	324,1	87,8
MD12-3417	Unit 1	1409,6	466,42	1,158	1,026	1,192	0,688	340	15,6	249,4	2,1	151,8	74,3
MD12-3417	Unit 1	1415,5	500,17	1,09	1,039	1,136	0,389	27,7	10,6	119,4	8,9	248,7	76,1
MD12-3417	Unit 1	1420,2	260,43	1,142	1,003	1,168	0,956	306,9	0,3	36,9	5	213,4	85
MD12-3417	Unit 1	1427,3	272,05	1,104	1,01	1,128	0,825	83,3	1,3	173,3	1,8	316,2	87,8
MD12-3417	Unit 1	1439,2	392,06	1,161	1,018	1,202	0,786	126	3,4	216	0,7	317,2	86,6
MD12-3417	Unit 1	1451	352,64	1,158	1,009	1,191	0,883	271,2	0,4	181,2	1,3	20,1	88,6
MD12-3417	Unit 1	1475,8	255,53	1,14	1,003	1,166	0,954	9,8	1,2	279,7	3,6	117,7	86,2
MD12-3417	Unit 1	1462,9	275,61	1,104	1,01	1,128	0,812	117,5	1	207,6	4	13,3	85,8
MD12-3417	Unit 1	1467,6	257,78	1,136	1,009	1,165	0,865	292,6	3,9	22,6	0,9	125,4	86
MD12-3417	Unit 1	1474,7	390,05	1,141	1,003	1,167	0,959	237,8	3,2	147,6	4,7	1,8	84,4
MD12-3417	Unit 1	1476,5	395,48	1,172	1,013	1,211	0,845	302,1	1,2	32,1	1,4	172,7	88,1
MD12-3417	Unit 1	1485,4	249,53	1,128	1,003	1,151	0,953	290,1	2,9	20,1	0,1	111,1	87,1
MD12-3417	Unit 1	1498,4	253,51	1,105	1,004	1,125	0,931	88,7	0,9	358,6	2,7	197,9	87,1
MD12-3417	Unit 1	1506,7	231,35	1,132	1,003	1,156	0,961	114,2	0,1	24,2	2,6	205,9	87,4
MD12-3417	Unit 1	1511,4	255,05	1,14	1,014	1,174	0,802	284,8	2,3	15	3,7	163,6	85,6
MD12-3417	Unit 1	1516,1	241,04	1,112	1,003	1,133	0,941	257,1	5,2	347,2	1,8	96,2	84,5

Core name	Unit	Composite depth (cm)	Km (10^{-6} SI)	F	L	Pj	T	K_1 dec	K_1 inc	K_2 dec	K_2 inc	K_3 dec	K_3 inc
MD12-3417	Unit 1	1522,1	263,05	1,092	1,008	1,112	0,831	268,8	1,2	358,8	0,3	104,3	88,7
MD12-3417	Unit 1	1535,7	320,29	1,107	1,012	1,133	0,791	283,4	3,3	13,6	3,3	148,4	85,4
MD12-3417	Unit 1	1537,5	234,69	1,136	1,002	1,16	0,966	55,8	0,2	145,8	1,1	314,4	88,9
MD12-3417	Unit 1	1544	341,82	1,093	1,018	1,121	0,667	281,3	0,1	191,3	4,4	13,1	85,6
MD12-3417	Unit 1	1545,2	287,87	1,138	1,012	1,17	0,826	135,8	0,9	225,8	2,7	26,3	87,1
MD12-3417	Unit 1	1550,5	438,53	1,177	1,013	1,217	0,858	310	5,8	219,8	1,9	111,4	83,9
MD12-3417	Unit 1	1555,8	335,09	1,123	1,01	1,15	0,842	126,8	3,4	36,3	7,3	241,4	81,9
MD12-3417	Unit 1	1561,1	243,13	1,136	1,003	1,155	0,958	338,9	2,3	248,8	3,1	105,5	86,2
MD12-3417	Unit 1	1567,7	333,89	1,082	1,013	1,105	0,724	260,9	1,9	170,6	6,8	6,6	83
MD12-3417	Unit 1	1569,4	290,77	1,142	1,005	1,169	0,926	302,9	1,7	32,9	0,9	151,3	88
MD12-3417	Unit 1	1573	352,41	1,177	1,009	1,213	0,893	328,6	2,1	58,7	1,9	190,8	87,1
MD12-3417	Unit 1	1579,5	297,6	1,09	1,014	1,115	0,72	123,6	2,6	213,7	2,9	351,8	86,2
MD12-3417	Unit 1	1591,3	323,4	1,104	1,008	1,126	0,858	258	0,5	167,9	1,8	4,1	88,1
MD12-3417	Unit 1	1593,1	329,27	1,15	1,002	1,17	0,978	351,5	2	81,5	2,4	221,5	86,9
MD12-3417	Unit 1	1603,2	300,59	1,076	1,01	1,095	0,75	295,7	5,3	26,3	6,4	166,4	81,6
MD12-3417	Unit 1	1606,1	280,36	1,15	1,002	1,185	0,976	7,7	0,5	277,7	4,3	104,3	85,7
MD12-3417	Unit 1	1615	330,37	1,11	1,008	1,134	0,851	86,4	2	176,4	1,9	310,1	87,3
MD12-3417	Unit 1	1626,9	272,56	1,082	1,002	1,096	0,962	240,7	5,3	150	7,6	5,3	80,7
MD12-3417	Unit 1	1638,7	263,29	1,082	1,006	1,105	0,863	310,9	2,5	220,7	4,5	69,5	84,8
MD12-3417	Unit 1	1650,5	314,7	1,135	1,012	1,166	0,831	123,6	5,9	213,9	3,3	332,8	83,2
MD12-3417	Unit 1	1652,9	307,72	1,162	1,006	1,202	0,931	332,4	1,8	62,5	1,9	199,5	87,4
MD12-3417	Unit 1	1667,7	250,64	1,135	1,002	1,161	0,975	241,8	1,6	331,9	1,3	100,3	88
MD12-3417	Unit 1	1674,2	270,78	1,1	1,004	1,119	0,912	261,3	0,3	171,3	3,6	355,9	86,4
MD12-3417	Unit 1	1677,8	226,25	1,072	1,003	1,085	0,907	256,4	2,9	166,4	1,2	53,9	86,9
MD12-3417	Unit 1	1684,9	219,52	1,093	1,006	1,112	0,883	293,8	2,1	203,8	0,7	96	87,8
MD12-3417	Unit 1	1697,9	348,64	1,122	1,016	1,153	0,758	113,8	0,9	203,9	3,1	7,3	86,8
MD12-3417	Unit 1	1699,1	254,04	1,162	1,007	1,197	0,918	340,1	1,9	70,1	0,6	176,9	88
MD12-3417	Unit 1	1706,2	376,77	1,183	1,005	1,215	0,939	16,2	1,5	106,2	0,2	205	88,4
MD12-3417	Unit 1	1712,7	249,79	1,053	1,007	1,066	0,753	325,8	1,6	235,8	0,6	126,2	88,4
MD12-3417	Unit 1	1715,1	274,82	1,10	1,017	1,13	0,695	165,8	1,4	75,5	10,	263,4	79,3

Core name	Unit	Composite depth (cm)	Km (10^{-6} SI)	F	L	Pj	T	K_1 dec	K_1 inc	K_2 dec	K_2 inc	K_3 dec	K_3 inc
MD12-3417	Unit 1	1719,8	247,04	1,143	1,003	1,169	0,963	259,5	3,8	169,5	0,1	77,6	86,2
MD12-3417	Unit 1	1726,9	240,6	1,192	1,004	1,227	0,959	217,1	0,8	307,2	3,9	115	86
MD12-3417	Unit 1	1732,8	344,64	1,148	1,01	1,18	0,862	106,9	3,9	197	1	301,1	86
MD12-3417	Unit 1	1734	302,65	1,186	1,005	1,221	0,948	189,9	0	279,9	1,3	97,8	88,7
MD12-3417	Unit 1	1736,4	286,18	1,161	1,003	1,19	0,965	2,9	1,5	93	2,1	238,6	87,4
MD12-3417	Unit 1	1744,7	315,46	1,11	1,006	1,132	0,898	236,5	1,7	146,4	2,2	3,2	87,2
MD12-3417	Unit 1	1749,4	190,48	1,169	1,007	1,203	0,919	244,2	4,6	334,3	1,5	82,2	85,1
MD12-3417	Unit 1	1756,5	320,13	1,102	1,005	1,122	0,909	96,3	0,1	186,3	5	5,1	85
MD12-3417	Unit 1	1761,3	320,22	1,136	1,005	1,163	0,919	215,7	1,1	305,8	4,1	109,9	85,8
MD12-3417	Unit 1	1773,1	279,54	1,164	1,003	1,194	0,955	217,4	2,5	307,6	4,1	95,9	85,2
MD12-3417	Unit 1	1780,2	298,86	1,134	1,005	1,16	0,92	89,8	1,9	179,8	2	315,5	87,2
MD12-3417	Unit 1	1785,5	226,21	1,121	1,003	1,143	0,969	192,8	0,9	282,9	6,5	94,5	83,4
MD12-3417	Unit 1	1792,1	367,37	1,16	1,007	1,131	0,873	262,1	0,1	352,1	0	91,5	89,9
MD12-3417	Unit 1	1796,8	300,56	1,156	1,002	1,183	0,979	306,8	3,2	216,8	0,5	118,2	86,8
MD12-3417	Unit 1	1803,9	325,39	1,125	1,006	1,15	0,908	260,3	0,2	170,3	4,6	352,4	85,4
MD12-3417	Unit 1	1810,4	261,34	1,143	1,001	1,168	0,981	295	3,6	25	0,1	116,1	86,4
MD12-3417	Unit 1	1815,7	291,15	1,131	1,004	1,155	0,944	117,2	4,6	207,5	3,2	332,7	84,4
MD12-3417	Unit 1	1820,5	247,7	1,115	1,003	1,135	0,951	281,8	0,4	11,8	2,4	183,3	87,5
MD12-3417	Unit 1	1827,6	314,22	1,105	1,002	1,124	0,96	273,2	1,5	183,1	4,8	21	85
MD12-3417	Unit 1	1841,8	309,28	1,12	1,009	1,146	0,852	242,4	4,2	332,6	3	98,6	84,8
MD12-3417	Unit 1	1851,3	387,04	1,111	1,005	1,132	0,904	239,9	0,3	149,9	4,7	333,9	85,3
MD12-3417	Unit 1	1863,1	393,63	1,082	1,013	1,104	0,721	9,5	3,1	100	8,6	259,8	80,8
MD12-3417	Unit 1	1865,5	333,61	1,129	1,019	1,164	0,737	261,7	0,2	351,7	11	170,6	79
MD12-3417	Unit 1	1870,2	380,56	1,158	1,014	1,195	0,827	358,2	9,7	268	1,4	169,6	80,2
MD12-3417	Unit 1	1874,9	481,68	1,115	1,013	1,143	0,786	5,3	2,6	96,5	24,4	269,6	65,5
MD12-3417	Unit 1	1877,3	392,86	1,142	1,011	1,173	0,852	58,3	8,7	326,6	10,9	186,4	76
MD12-3417	Unit 1	1882	400,4	1,155	1,009	1,187	0,887	296,1	12,2	29,8	16,5	171,4	69,2
MD12-3417	Unit 1	1892,7	474,78	1,141	1,0205	1,179	0,7275	229,65	6,8	139,2	4,1	198,5	82,05
MD12-3417	Unit 1	1898,6	528,38	1,13	1,037	1,191	0,564	119,8	10,	28	9,6	255,4	75,9

Core name	Unit	Composite depth (cm)	Km (10^{-6} SI)	F	L	Pj	T	K_1 dec	K_1 inc	K_2 dec	K_2 inc	K_3 dec	K_3 inc
MD12-3417	Unit 1	1901,6	423,58	1,179	1,017	1,218	0,813	309,6	6,8	39,9	2,3	148,5	82,9
MD12-3417	Unit 1	1910,5	280,99	1,089	1,008	1,108	0,833	105,9	0,2	196	3,7	13,2	86,3
MD12-3417	Unit 1	1917	215,35	1,092	1,002	1,108	0,957	321,5	3,2	231,4	1,5	116,2	86,5
MD12-3417	Unit 1	1927	248,95	1,137	1,003	1,162	0,956	318,2	1,2	228,1	2,4	74,1	87,3
MD12-3417	Unit 1	1934,1	245,25	1,064	1,005	1,078	0,841	119,1	2,5	209,2	2,7	346,1	86,3
MD12-3417	Unit 1	1944,2	243,84	1,1	1,003	1,118	0,935	301,6	0,5	211,6	0,8	61,9	89
MD12-3417	Unit 1	1953,1	232,81	1,126	1,003	1,149	0,951	328,4	2,1	238,3	1,7	108,6	87,3
MD12-3417	Unit 1	1957,8	319,83	1,1	1,009	1,122	0,875	99,7	0,7	9,7	1,3	219,4	88,5
MD12-3417	Unit 1	1964,9	311,8	1,136	1,005	1,163	0,921	258,3	3,6	168,3	0,3	73,1	86,4
MD12-3417	Unit 1	1975,6	320,56	1,159	1,001	1,197	0,986	118,3	0,1	208,3	4,2	26,3	85,8
MD12-3417	Unit 1	1981,5	468,95	1,15	1,012	1,184	0,844	120,7	1,8	210,7	0,7	321,7	88,1
MD12-3417	Unit 1	1983,9	349,75	1,206	1,013	1,251	0,873	323,1	2,6	53,4	5,2	206,4	84,2
MD12-3417	Unit 1	1986,8	436,06	1,23	1,01	1,279	0,905	311,7	4,2	41,8	1,4	150,6	85,6
MD12-3417	Unit 1	1993,4	310,35	1,168	1,008	1,131	0,851	265,4	1,8	175,4	1,2	50,5	87,8
MD12-3417	Unit 1	1999,3	258,47	1,128	1,002	1,15	0,971	221,4	2	131,4	0,5	28,1	88
MD12-3417	Unit 1	2011,1	307,02	1,135	1,004	1,16	0,943	245,4	0,7	155,4	0,4	32	89,2
MD12-3417	Unit 1	2023	313,1	1,178	1,006	1,212	0,931	304,1	1,2	34,2	0,7	154	88,6
MD12-3417	Unit 1	2034,6	254,29	1,114	1,003	1,135	0,943	296,3	1	206,3	0,2	102,6	88,9
MD12-3417	Unit 1	2046,6	245,4	1,098	1,002	1,116	0,949	300,8	2,2	30,8	0,1	122,8	87,8
MD12-3417	Unit 1	2058,5	320,65	1,164	1,009	1,199	0,891	322,7	1	52,7	0,9	184,3	88,7
MD12-3417	Unit 1	2065	282,27	1,135	1,01	1,16	0,846	324,7	0,5	234,7	0	143,7	89,5
MD12-3417	Unit 1	2076,8	267,66	1,156	1,005	1,186	0,931	294,4	2,1	24,5	3	170,2	86,3
MD12-3417	Unit 1	2088,7	272,25	1,153	1,002	1,179	0,975	342,1	1,3	72,1	0,4	180,8	88,6
MD12-3417	Unit 1	2100,5	282,05	1,149	1,002	1,175	0,973	261,8	0,8	351,8	1	132,3	88,7
MD12-3417	Unit 1	2112,4	272,23	1,118	1,001	1,138	0,981	259,7	1,2	349,8	2,2	140,7	87,5
MD12-3417	Unit 1	2124,2	265,13	1,144	1,001	1,169	0,985	217,1	1,4	307,2	5	111,2	84,8
MD12-3417	Unit 1	2136	334,67	1,188	1,003	1,222	0,965	309,7	4,3	219,7	0,2	126,6	85,7
MD12-3417	Unit 1	2147,9	269,82	1,119	1,006	1,143	0,9	255,5	2,3	345,5	0,9	95,8	87,6
MD12-3417	Unit 1	2159,7	254,89	1,10	1,005	1,129	0,915	236,2	4,1	326,5	3,9	99,8	84,4

Core name	Unit	Composite depth (cm)	Km (10^{-6} SI)	F	L	Pj	T	K_1 dec	K_1 inc	K_2 dec	K_2 inc	K_3 dec	K_3 inc
MD12-3417	Unit 1	2171,6	251,07	1,098	1,009	1,121	0,826	233,7	0,5	143,7	0,9	355,1	89
MD12-3417	Unit 1	2183,4	297,39	1,117	1,006	1,140	0,888	306,4	1,6	216,25	2,8	70,45	86,65
MD12-3417	Unit 1	2195,3	260,59	1,137	1,014	1,169	0,805	202,9	2,7	293,1	2,4	63,9	86,4
MD12-3417	Unit 1	2207,1	275,64	1,119	1,005	1,142	0,918	104,8	0,3	14,8	3,4	200,6	86,6
MD12-3417	Unit 1	2218,9	260,92	1,147	1,002	1,173	0,968	270	1,4	0	1,8	142,5	87,7
MD12-3417	Unit 1	2230,8	270,91	1,114	1,006	1,1365	0,9035	196,9	2	186,9	0,35	185,15	88
MD12-3417	Unit 1	2243,2	227,71	1,105	1,002	1,123	0,961	14,9	2,1	284,8	1,2	164,4	87,5
MD12-3417	Unit 1	2251,5	271,16	1,16	1,004	1,19	0,945	11,7	1	281,6	5,5	112,3	84,4
MD12-3417	Unit 1	2258,6	228,68	1,133	1,002	1,156	0,875	268,8	2,7	178,8	0,2	85,5	87,3
MD12-3417	Unit 1	2265,7	245,44	1,101	1,01	1,124	0,815	256,4	4,1	166,4	1	63,1	85,8
MD12-3417	Unit 1	2275,2	265,18	1,134	1,004	1,159	0,934	67	1,3	157	3,3	315,5	86,4
MD12-3417	Unit 1	2283,5	251,96	1,107	1,013	1,133	0,789	195,2	2,1	285,4	3,8	76,2	85,6
MD12-3417	Unit 1	2285,8	201,57	1,11	1,012	1,149	0,817	189,3	0,5	99,3	0,4	331,8	89,4
MD12-3417	Unit 1	2288,2	255,96	1,111	1,016	1,146	0,748	184,2	0,2	94,2	2,8	278	87,2
MD12-3417	Unit 1	2290,6	311,71	1,138	1,003	1,164	0,949	247,7	3,7	337,8	2,2	98,9	85,7
MD12-3417	Unit 1	2292,9	302,34	1,153	1,004	1,182	0,939	197,4	2,6	107,3	2,3	335,7	86,5
MD12-3417	Unit 1	2295,3	320,61	1,156	1,003	1,185	0,956	92,2	0,5	2,2	5,1	188,4	84,9
MD12-3417	Unit 1	2297,7	310,37	1,129	1,016	1,162	0,771	142,1	1,3	52	2,4	259,9	87,3
MD12-3417	Unit 1	2300,1	285,7	1,117	1,016	1,148	0,749	297,8	1,9	207,8	0,5	103,2	88
MD12-3417	Unit 1	2302,4	360,98	1,148	1,009	1,179	0,873	319,4	5,4	228,8	6,4	89,2	81,7
MD12-3417	Unit 1	2304,8	404,2	1,166	1,013	1,204	0,848	92,9	4	2,6	3,8	229,6	84,5
MD12-3417	Unit 1	2307,2	436,99	1,12	1,017	1,153	0,738	78,6	0,3	348,6	8,6	170,4	81,4
MD12-3417	Unit 1	2309,5	519,57	1,142	1,02	1,181	0,742	129,6	3,5	39,3	4	260,7	84,7
MD12-3417	Unit 1	2311,9	436,73	1,171	1,026	1,22	0,723	141,2	4,1	50,9	4,6	273,3	83,8
MD12-3417	Unit 1	2314,3	293,97	1,135	1,005	1,16	0,925	71,6	6,5	341	5,1	213,4	81,7
MD12-3417	Unit 1	2316,6	264,28	1,079	1,04	1,124	0,318	72	8,7	341,7	1,4	242,4	81,1
MD12-3417	Unit 1	2319	317,83	1,151	1,001	1,177	0,981	342,3	5,7	72,8	5	203,7	82,4
MD12-3417	Unit 1	2323,7	316,7	1,149	1,014	1,184	0,816	104	0,9	13,9	5,8	203,1	84,1

Core name	Unit	Composite depth (cm)	Km (10^{-6} SI)	F	L	Pj	T	K_1 dec	K_1 inc	K_2 dec	K_2 inc	K_3 dec	K_3 inc
MD12-3417	Unit 1	2326,1	287,3	1,149	1,002	1,176	0,965	346,2	4,3	76,5	2,9	200,4	84,8
MD12-3417	Unit 1	2328,5	281,81	1,148	1,013	1,182	0,833	19,1	5,3	109,3	2	219,7	84,3
MD12-3417	Unit 1	2330,8	242,69	1,074	1,003	1,088	0,909	32,2	2	302,1	1,9	169,4	87,3
MD12-3417	Unit 1	2339,1	253,94	1,12	1,004	1,142	0,931	303,2	5,7	213,1	1,3	109,9	84,1
MD12-3417	Unit 1	2347,4	234,28	1,089	1,001	1,104	0,981	281,7	2,5	11,8	0,8	119,4	87,4
MD12-3417	Unit 1	2354,5	266,35	1,135	1,001	1,158	0,978	325	2,9	234,8	3,9	91,1	85,2
MD12-3417	Unit 1	2364	257,68	1,137	1,004	1,162	0,944	2[illegible]4	4	5,4	1,1	110,4	85,9
MD12-3417	Unit 1	2372,3	291,11	1,164	1,006	1,195	0,928	314,3	3,5	224,2	1,2	115,4	86,3
MD12-3417	Unit 1	2380,6	261,81	1,126	1,004	1,149	0,912	346,4	2,5	76,5	2	205,2	86,8
MD12-3417	Unit 1	2388,9	251,7	1,137	1,004	1,162	0,945	289,5	2,1	199,5	0,1	105,7	87,9
MD12-3417	Unit 1	2397,2	288,97	1,128	1,01	1,156	0,853	321	5,4	230,7	3,5	108,4	83,6
MD12-3417	Unit 1	2405,4	260,78	1,108	1,005	1,129	0,909	341,5	0,6	251,5	1,4	94,1	88,5
MD12-3417	Unit 1	2413,7	260,17	1,105	1,009	1,128	0,832	240,6	5,5	330,7	1,8	78,7	84,2
MD12-3417	Unit 1	2419,7	269,95	1,107	1,007	1,129	0,878	258,7	6,5	168,6	0,2	76,7	83,5
MD12-3417	Unit 1	2427,9	261,16	1,131	1,003	1,13	0,935	316,2	4	225,9	4,5	88,1	84
MD12-3417	Unit 1	2444,5	285,05	1,132	1,014	1,164	0,798	264,8	4,4	174,7	1,6	64,5	85,3
MD12-3417	Unit 1	2452,8	290,3	1,163	1,004	1,192	0,954	249,7	1,7	339,8	4,9	140,9	84,8
MD12-3417	Unit 1	2461,1	418,11	1,212	1,027	1,27	0,755	322,5	6	52,9	4,1	177,3	82,7
MD12-3417	Unit 1	2469,4	211,27	1,074	1,001	1,092	0,976	335,9	2,7	66,1	3,3	206,7	85,7
MD12-3417	Unit 1	2477,7	278,07	1,144	1,002	1,173	0,969	299,3	1,7	29,3	0,4	134,1	88,3
MD12-3417	Unit 1	2494,3	248,31	1,114	1,021	1,149	0,686	206,1	0,9	296,1	1,9	90,4	87,9
MD12-3417	Unit 1	2502,5	259,43	1,113	1,007	1,136	0,879	200,3	2,1	290,5	4,8	86,7	84,8
MD12-3417	Unit 1	2510,8	277,4	1,134	1,006	1,16	0,912	293,1	1,8	203,1	1,8	68,1	87,5
MD12-3417	Unit 1	2519,1	374,62	1,154	1,014	1,19	0,819	321,6	8,2	231,3	2,4	125,2	81,5
MD12-3417	Unit 1	2526,2	426,28	1,191	1,018	1,237	0,818	305,3	7,9	36,6	9	174,8	78
MD12-3417	Unit 1	2534,5	244,85	1,118	1,002	1,139	0,96	309,2	1	39,3	1,6	187	88,1
MD12-3417	Unit 1	2542,8	230,04	1,114	1,012	1,141	0,798	268,2	4,5	358,5	4,3	132,1	83,8
MD12-3417	Unit 1	2551,1	264,66	1,122	1,007	1,147	0,883	234,3	2,1	324,4	4,7	120,6	84,8
MD12-3417	Unit 1	2559,4	250,2	1,099	1,021	1,131	0,639	359	3,4	268,7	5,1	122,3	83,8

Core name	Unit	Composite depth (cm)	Km (10^{-6} SI)	F	L	Pj	T	K_1 dec	K_1 inc	K_2 dec	K_2 inc	K_3 dec	K_3 inc
MD12-3417	Unit 1	2567,7	294,39	1,134	1,006	1,16	0,914	246,5	0,6	336,5	4,8	149	85,2
MD12-3417	Unit 1	2570	328,28	1,14	1,007	1,168	0,903	121,4	2,1	31,3	1,5	266	87,4
MD12-3417	Unit 1	2576	421,54	1,18	1,022	1,227	0,769	317,8	8,8	48,3	3,5	159,9	80,5
MD12-3417	Unit 1	2578,3	402,16	1,19	1,019	1,236	0,809	310,4	8,7	42	9,9	179,6	76,8
MD12-3417	Unit 1	2580,7	430,03	1,179	1,024	1,229	0,745	317,9	7,6	49,3	10,4	192,3	77,1
MD12-3417	Unit 1	2583,1	454,1	1,17	1,026	1,219	0,723	317,5	9,8	49	8,9	180,6	76,7
MD12-3417	Unit 1	2585,4	539,52	1,135	1,007	1,162	0,89	349,9	17,8	259,9	0,1	169,6	72,2
MD12-3417	Unit 1	2587,8	322,64	1,135	1,001	1,158	0,982	3[illegible]1	10	87,6	2,7	192,8	79,6
MD12-3417	Unit 1	2590,2	228,51	1,114	1,004	1,136	0,936	357,7	7,3	267,5	1,5	165,8	82,5
MD12-3417	Unit 1	2592,5	254,31	1,14	1,002	1,165	0,966	29,8	3,8	299,4	7,1	147,8	81,9
MD12-3417	Unit 1	2594,9	259,63	1,114	1,003	1,134	0,954	2,9	4,2	272,6	4	139,6	84,2
MD12-3417	Unit 1	2600,2	252,29	1,12	1,002	1,141	0,965	318,9	3,3	48,9	0	139,1	86,7
MD12-3417	Unit 1	2606,2	228,48	1,127	1,003	1,15	0,955	42,1	1,1	312,1	0,8	186,6	88,6
MD12-3417	Unit 1	2612,1	232,91	1,129	1,005	1,153	0,926	265,1	4,5	355,3	2,7	116,3	84,8
MD12-3417	Unit 1	2618	279,78	1,164	1,003	1,194	0,966	241,8	4,1	332,1	4,5	109,8	83,9
MD12-3417	Unit 1	2622,7	356,62	1,186	1,007	1,222	0,925	252,8	4,5	343,2	4,6	118,6	83,6
MD12-3417	Unit 1	2629,8	239,16	1,124	1,002	1,146	0,963	12,1	5,4	282	0,9	182,9	84,6
MD12-3417	Unit 1	2635,8	249,64	1,154	1,003	1,182	0,954	218,9	0,3	308,9	4,4	125,3	85,6
MD12-3417	Unit 1	2641,7	263,41	1,177	1,003	1,209	0,965	80,9	1	350,8	6	180,3	83,9
MD12-3417	Unit 1	2646,4	295,95	1,236	1,013	1,287	0,888	264,4	8,2	355,4	6,9	124,7	79,2
MD12-3417	Unit 1	2652,3	232,5	1,107	1,001	1,125	0,985	312,6	4,2	42,8	2,7	165,3	85,1
MD12-3417	Unit 1	2658,3	229,8	1,133	1,004	1,158	0,939	27,1	2	297	3,4	147,8	86
MD12-3417	Unit 1	2670,1	284,77	1,145	1,006	1,173	0,917	232,5	0,2	322,6	4,4	139,5	85,6
MD12-3417	Unit 1	2676	204,6	1,092	1,003	1,109	0,934	240,4	1,5	330,5	4,2	131	85,6
MD12-3417	Unit 1	2681,9	288,58	1,157	1,003	1,186	0,954	237,9	1,1	328	2,6	124,7	87,2
MD12-3417	Unit 1	2687,9	351,82	1,178	1,01	1,215	0,888	230,2	0,7	320,2	5,6	133,6	84,3
MD12-3417	Unit 1	2693,8	279,13	1,171	1,005	1,203	0,944	243,9	1,7	333,9	0,2	71,1	88,3
MD12-3417	Unit 1	2699,7	234,9	1,099	1,003	1,117	0,939	50,9	0,4	320,9	2,9	149,7	87,1
MD12-3417	Unit 1	2705,6	317,37	1,161	1,005	1,192	0,935	236,8	0,2	326,8	3,8	143,2	86,2
MD12-3417	Unit 1	2711,5	250,74	1,131	1,004	1,155	0,939	326,3	2,7	56,3	1,6	176,2	86,8

Core name	Unit	Composite depth (cm)	Km (10^{-6} SI)	F	L	Pj	T	K_1 dec	K_1 inc	K_2 dec	K_2 inc	K_3 dec	K_3 inc
MD12-3417	Unit 1	2717,5	269,05	1,111	1,01	1,137	0,82	300,5	3,4	30,5	0,3	126,2	86,6
MD12-3417	Unit 1	2723,4	250,72	1,094	1,018	1,123	0,665	303,1	3,5	33,1	0,3	128	86,5
MD12-3417	Unit 1	2729,3	220,33	1,119	1,011	1,146	0,825	320,3	3,8	230,1	1,8	114,3	85,8
MD12-3417	Unit 1	2735,2	237,96	1,17	1,005	1,202	0,94	236,7	0,1	326,7	2,6	145,6	87,4
MD12-3417	Unit 1	2741,2	277,17	1,177	1,003	1,21	0,962	93,1	0,8	3	3,6	195	86,4
MD12-3417	Unit 1	2747,1	281,61	1,141	1,008	1,17	0,891	15,4	3,6	285,1	3,3	152,3	85,1
MD12-3417	Unit 1	2753	217,35	1,109	1,001	1,127	0,984	99,6	0,5	0,6	2,5	192,2	87,5
MD12-3417	Unit 1	2758,9	239,82	1,141	1,003	1,166	0,958	234,4	0	324,4	2,6	144,1	87,4
MD12-3417	Unit 1	2764,8	258,68	1,113	1,009	1,138	0,843	75,5	0,3	165,5	0,2	293	89,6
MD12-3417	Unit 1	2770,8	270,1	1,101	1,015	1,125	0,754	50	0,2	140	2,1	315,7	87,9
MD12-3417	Unit 1	2775,5	272,41	1,106	1,008	1,123	0,853	85,1	1,4	175,2	4,1	336,8	85,7
MD12-3417	Unit 1	2781,4	261,68	1,151	1,006	1,118	0,924	147,5	1,6	57,4	5,5	254	84,3
MD12-3417	Unit 1	2787,3	336,08	1,187	1,004	1,222	0,959	56,5	3,1	326,5	1,1	216,1	86,7
MD12-3417	Unit 1	2793,3	406,96	1,23	1,005	1,273	0,957	256,2	1	346,3	6,6	157,5	83,3
MD12-3417	Unit 1	2799,2	262,85	1,129	1,005	1,154	0,925	73,8	1,2	343,8	0,3	238,2	88,8
MD12-3417	Unit 1	2805,1	226,83	1,099	1,001	1,106	0,985	264,6	1,8	354,7	2,3	136,5	87,1
MD12-3417	Unit 1	2811	277,75	1,112	1,001	1,131	0,98	40,7	0,5	310,7	0,7	163,1	89,1
MD12-3417	Unit 1	2816,9	230,78	1,08	1	1,094	0,994	14,8	2	284,7	4,2	130,3	85,3
MD12-3417	Unit 1	2822,9	298,71	1,114	1,002	1,134	0,963	60,8	2,5	330,6	3,1	189,2	86
MD12-3417	Unit 1	2828,8	302,56	1,14	1,008	1,169	0,888	255	2,5	345,1	1,8	111,1	86,9
MD12-3417	Unit 1	2834,7	259,06	1,09	1,001	1,105	0,975	261,8	0,7	351,9	4	162,1	86
MD12-3417	Unit 1	2840,6	241,56	1,091	1,001	1,106	0,973	310,4	1,5	40,5	0,7	156	88,3
MD12-3417	Unit 1	2846,5	286,28	1,141	1,004	1,168	0,936	248,7	0,4	338,7	3,7	152,7	86,3
MD12-3417	Unit 1	2852,5	235,11	1,101	1,001	1,119	0,976	112,6	0	22,6	3,3	203,1	86,7
MD12-3417	Unit 1	2858,4	255,77	1,136	1,004	1,162	0,94	258,7	0,7	348,7	2,9	154,3	87
MD12-3417	Unit 1	2864,3	216,67	1,082	1,001	1,096	0,971	266,9	0,4	356,9	3,1	170,1	86,9
MD12-3417	Unit 1	2870,2	239,58	1,133	1,004	1,157	0,941	40,6	1,6	310,5	1,1	185,6	88,1
MD12-3417	Unit 1	2876,1	259,72	1,127	1,005	1,152	0,92	276,3	1,8	6,3	1,3	132,6	87,7
MD12-3417	Unit 1	2882,1	249,78	1,127	1,002	1,15	0,96	51,5	1	321,4	3,3	158,2	86,6
MD12-3417	Unit 1	2888	226,99	1,127	1,006	1,152	0,906	122	0,7	31,9	4,4	221,2	85,5

Core name	Unit	Composite depth (cm)	Km (10^{-6} SI)	F	L	Pj	T	K_1 dec	K_1 inc	K_2 dec	K_2 inc	K_3 dec	K_3 inc
MD12-3417	Unit 1	2893,9	255,24	1,11	1,011	1,135	0,809	283,1	1,3	13,2	2,1	160,4	87,5
MD12-3417	Unit 1	2899,8	259,14	1,10 6	1,008	1,129	0,849	321,7	2,9	51,7	1,4	167,4	86,8
MD12-3417	Unit 1	2905,7	267,22	1,12	1,001	1,141	0,986	213,8	1,1	303,8	0,1	37,1	88,9
MD12-3417	Unit 1	2911,7	283,8	1,10 7	1,009	1,131	0,836	41,1	0,8	131,1	4	300,3	85,9
MD12-3417	Unit 1	2917,6	304,41	1,11 8	1,008	1,144	0,861	215,1	2,7	305,1	1,8	68,4	86,7
MD12-3417	Unit 1	2923,5	344,29	1,17 2	1,004	1,203	0,956	293,8	3,4	24	3,4	158,8	85,2
MD12-3417	Unit 1	2929,4	398,98	1,17 8	1,004	1,212	0,952	96,5	2,2	6,2	5,8	206,9	83,8
MD12-3417	Unit 1	2935,4	336,96	1,16 8	1,005	1,2	0,942	60,6	1,1	330,5	5,3	162	84,6
MD12-3417	Unit 1	2941,3	252,02	1,13 2	1,003	1,155	0,952	60,5	4,1	330,3	3,3	201,8	84,7
MD12-3417	Unit 1	2947,2	208,45	1,12 8	1,003	1,151	0,956	264,5	0,1	354,5	3,1	173,1	86,9
MD12-3417	Unit 1	2957,9	272,76	1,10 4	1,015	1,132	0,74	230,1	2,1	320,2	2,8	103,2	86,5
MD12-3417	Unit 1	2969,7	291,14	1,11 3	1,005	1,136	0,905	325,3	1,3	55,3	1,3	189,6	88,2
MD12-3417	Unit 1	2975,6	329,31	1,14 9	1,007	1,18	0,902	317,4	1,2	47,5	1,4	186,2	88,2
MD12-3417	Unit 1	2981,5	339,57	1,26 9	1,019	1,332	0,851	304,9	8,9	36,1	7,6	165,9	78,2
MD12-3417	Unit 1	2987,5	538,83	1,22 1	1,025	1,278	0,782	312,3	10, 2	43,9	8,4	172,5	76,7
MD12-3417	Unit 1	2993,4	261,84	1,13 1	1,002	1,155	0,961	304,5	4,1	34,8	3,8	167,4	84,4
MD12-3417	Unit 1	2999,3	255,5	1,12 5	1,003	1,148	0,947	273,9	1,8	4	5,3	165	84,4
MD12-3417	Unit 1	3005,2	250,07	1,12	1,003	1,141	0,952	277,6	2,9	7,9	5,1	158	84,1
MD12-3417	Unit 1	3011,1	252,55	1,13	1,002	1,152	0,973	295	5,2	25	1	126,5	84,7
MD12-3417	Unit 1	3017,1	275,39	1,10 8	1,008	1,132	0,849	266	2,9	356,1	2	120,3	86,4
MD12-3417	Unit 1	3023	290,08	1,13 9	1,005	1,166	0,933	289,6	2,4	19,7	2	150,1	86,8
MD12-3417	Unit 1	3028,9	345,36	1,15	1,006	1,179	0,92	278,5	2,6	8,6	3,7	153,8	85,5
MD12-3417	Unit 1	3034,8	310,32	1,14 6	1,003	1,172	0,953	274,4	1,4	4,5	4,5	166,9	85,3
MD12-3417	Unit 1	3040,7	307,34	1,15 7	1,004	1,186	0,951	268,1	2,2	358,2	3,2	143,2	86,1
MD12-3417	Unit 1	3046,7	245,41	1,11 3	1,001	1,132	0,99	236,6	1,3	326,7	2,7	121	87
MD12-3417	Unit 1	3052,6	247,23	1,12 9	1,001	1,151	0,982	282	4,8	12,1	1,9	123,4	84,9
MD12-3417	Unit 1	3058,5	267,09	1,12 6	1,005	1,15	0,926	4,5	0,6	274,4	6,7	99,4	83,3
MD12-3417	Unit 1	3064,4	292,52	1,14 9	1,006	1,178	0,918	267,5	5	357,8	4,2	127,9	83,5
MD12-3417	Unit 1	3069,2	352,16	1,17 1	1,005	1,204	0,936	290	3,2	20,1	2,5	148,5	86
MD12-3417	Unit 1	3075,1	386,45	1,17 9	1,012	1,218	0,867	303,6	6,8	34	3,2	149,3	82,4

Core name	Unit	Composite depth (cm)	Km (10^{-6} SI)	F	L	Pj	T	K_1 dec	K_1 inc	K_2 dec	K_2 inc	K_3 dec	K_3 inc
MD12-3417	Unit 1	3081	410,5	1,176	1,011	1,214	0,871	301,1	9,5	31,8	4,5	146,7	79,5
MD12-3417	Unit 1	3088,1	266,11	1,107	1,01	1,132	0,822	357,5	3,4	267,2	5,9	117	83,2
MD12-3417	Unit 1	3095,2	340,5	1,147	1,004	1,175	0,948	239	3,1	329,2	4,5	114,7	84,5
MD12-3417	Unit 1	3099,9	342,25	1,165	1,004	1,196	0,948	283	3,4	13,1	1,2	123,3	86,4
MD12-3417	Unit 1	3104,7	390,33	1,172	1,011	1,21	0,868	294,7	8,4	24,8	0,3	116,9	81,6
MD12-3417	Unit 1	3111,8	266,76	1,131	1,004	1,155	0,938	277,6	0,3	7,6	2,2	179,2	87,8
MD12-3417	Unit 1	3120,1	267,29	1,117	1,008	1,142	0,864	178,6	1,4	88,4	6,4	281,1	83,5
MD12-3417	Unit 1	3126	270,4	1,1	1,008	1,122	0,854	118,2	1,4	28,1	5	223,4	84,8
MD12-3417	Unit 1	3135,5	228,89	1,122	1,004	1,144	0,877	11	5	101,2	1,9	211,7	84,7
MD12-3417	Unit 1	3141,4	283,62	1,132	1,003	1,155	0,956	261,8	3,8	352,3	8,2	147,4	80,9
MD12-3417	Unit 1	3147,3	315,89	1,131	1,004	1,156	0,937	44,4	6,2	134,8	3,9	257,2	82,7
MD12-3417	Unit 1	3153,2	364,67	1,143	1,029	1,189	0,645	320,8	17,6	52,7	5,8	160,3	71,4
MD12-3417	Unit 1	3159,2	453,26	1,104	1,047	1,159	0,367	338,9	34,6	86	23,1	202,6	46,3
MD12-3417	Unit 1	3163,9	504,57	1,083	1,058	1,115	-0,033	346,5	50,7	90,9	11,5	189,7	37
MD12-3417	Unit 1	3167,4	417,94	1,094	1,01	1,119	0,796	315	2,1	45,6	17,3	218,3	72,5
MD12-3417	Unit 1	3176,9	257,01	1,116	1,005	1,138	0,919	231,8	1,3	321,9	6,6	130,9	83,2
MD12-3417	Unit 1	3182,8	305,42	1,139	1,005	1,165	0,925	241,2	1,5	331,3	5,1	135,4	84,7
MD12-3417	Unit 1	3188,6	276,03	1,099	1,005	1,119	0,906	14,7	2,8	284,4	4,9	134,7	84,3
MD12-3417	Unit 1	3194,7	309,67	1,129	1,003	1,152	0,948	241,7	0,6	331,8	7,2	146,7	82,7
MD12-3417	Unit 1	3200,6	245,68	1,091	1,004	1,108	0,913	88,2	2	358,1	3,2	211	86,2
MD12-3417	Unit 1	3206,5	256,01	1,125	1,004	1,149	0,933	45,3	0,3	315,3	2,8	140,8	87,2
MD12-3417	Unit 1	3212,4	264,94	1,106	1,012	1,133	0,782	34,8	2,3	304,6	3,1	161,5	86,1
MD12-3417	Unit 1	3218,4	283,94	1,151	1,007	1,181	0,909	249,2	0	339,2	2,8	158,9	87,2
MD12-3417	Unit 1	3224,3	299,84	1,149	1,005	1,178	0,936	259,9	1,2	350	3,4	151,3	86,4
MD12-3417	Unit 1	3229	241,04	1,105	1,004	1,125	0,926	68,5	1,2	338,4	2,8	181,1	87
MD12-3417	Unit 1	3236,1	266,26	1,107	1,012	1,133	0,786	350,2	0,5	80,2	0,4	211,2	89,3
MD12-3417	Unit 1	3242	237,72	1,124	1,004	1,148	0,93	230,8	0,1	320,8	0,9	132,5	89,1
MD12-3417	Unit 1	3248	280,05	1,119	1,002	1,14	0,963	80,4	0,4	170,4	0,4	301,9	89,4
MD12-3417	Unit 1	3253,9	303,42	1,132	1,004	1,157	0,931	248,8	0,3	338,8	2,1	150,6	87,9

Core name	Unit	Composite depth (cm)	Km (10^{-6} SI)	F	L	Pj	T	K_1 dec	K_1 inc	K_2 dec	K_2 inc	K_3 dec	K_3 inc
MD12-3417	Unit 1	3259,8	348,59	1,132	1,005	1,157	0,92	118,7	3,1	28,7	1,3	276,6	86,7
MD12-3417	Unit 1	3264,5	364,78	1,124	1,012	1,153	0,82	148,2	1,4	58,1	4,5	255	85,3
MD12-3417	Unit 1	3271,7	382,22	1,123	1,025	1,163	0,648	39,1	2,2	129,2	0,3	227,7	87,8
MD12-3417	Unit 1	3277,6	355,43	1,168	1,004	1,2	0,952	101,7	5,8	191,8	1,5	295,8	84
MD12-3417	Unit 1	3283,5	349,38	1,163	1,011	1,198	0,865	342,1	0,5	72,2	5,9	247,1	84,1
MD12-3417	Unit 1	3289,4	465,28	1,206	1,012	1,25	0,882	299,2	2,1	29,4	5,8	189	83,8
MD12-3417	Unit 1	3293	485,42	1,212	1,011	1,257	0,892	303,8	2,2	34,1	7,1	196,6	82,5
MD12-3417	Unit 1	3301,3	269,36	1,139	1,002	1,164	0,964	339,3	0,3	89,3	1,6	259,7	88,4
MD12-3417	Unit 1	3309,5	241,45	1,124	1,001	1,145	0,95	28,5	4,1	118,9	4,9	258,9	83,6
MD12-3417	Unit 1	3313,1	238,89	1,124	1,004	1,147	0,932	105,7	3,3	15,7	1,1	267,5	86,5
MD12-3417	Unit 1	3319	271,23	1,122	1,002	1,143	0,966	44,2	1,7	134,2	1,7	268,3	87,6
MD12-3417	Unit 1	3324,9	287,14	1,129	1,003	1,156	0,879	339,9	0,7	70	3,2	237,2	86,8
MD12-3417	Unit 1	3330,9	294,9	1,161	1,004	1,194	0,947	84,2	1,3	354,2	1,3	218,8	88,1
MD12-3417	Unit 1	3336,8	294,9	1,23	1,005	1,275	0,95	274,2	0,7	4,2	4	174,1	86
MD12-3417	Unit 1	3342,7	242,63	1,121	1,002	1,142	0,96	77	2	346,8	3,2	199,1	86,2
MD12-3417	Unit 1	3347,4	247,74	1,121	1,002	1,143	0,96	314	4,3	44,1	1,6	154,5	85,4
MD12-3417	Unit 1	3354,5	254,95	1,141	1,002	1,166	0,969	280,7	1,4	10,8	2,1	156	87,5
MD12-3417	Unit 1	3362,8	294,74	1,15	1,003	1,178	0,955	128	0,5	37,9	3,1	226,4	86,8
MD12-3417	Unit 1	3368,8	309,24	1,155	1,005	1,185	0,935	307,9	1,3	37,9	3,4	197,2	86,4
MD12-3417	Unit 1	3374,7	252,34	1,125	1,002	1,147	0,963	83	0,9	353	0,8	220,8	88,9
MD12-3417	Unit 1	3380,6	258,49	1,137	1,001	1,16	0,984	205	0,6	115	0,1	16,9	89,4
MD12-3417	Unit 1	3386,5	278,12	1,102	1,016	1,131	0,714	322,6	0,6	232,6	1	83	88,9
MD12-3417	Unit 1	3392,4	321,35	1,167	1,011	1,203	0,87	262,1	2,3	352,1	0,9	102,6	87,5
MD12-3417	Unit 1	3398,4	415,82	1,191	1,007	1,229	0,924	298,4	2,1	28,5	2,6	169,6	86,6
MD12-3417	Unit 1	3403,1	524,38	1,247	1,014	1,3	0,885	297,6	2,6	27,7	3,4	169,6	85,7
MD12-3417	Unit 1	3405,5	503,96	1,202	1,012	1,245	0,878	105,2	0,5	15,1	4	202,9	86
MD12-3417	Unit 1	3411,4	236,24	1,111	1,001	1,13	0,975	337,3	1,4	67,5	5,9	233,8	84
MD12-3417	Unit 1	3417,3	246,58	1,132	1,002	1,156	0,974	90,6	2,7	180,6	0,4	278	87,2
MD12-3417	Unit 1	3423,2	236,42	1,1	1,006	1,12	0,873	49,4	0,1	319,4	0,5	148,4	89,5

Core name	Unit	Composite depth (cm)	Km (10^{-6} SI)	F	L	Pj	T	K_1 dec	K_1 inc	K_2 dec	K_2 inc	K_3 dec	K_3 inc
MD12-3417	Unit 1	3426,8	323,16	1,124	1,003	1,147	0,944	94,6	0,7	184,6	2,7	349,9	87,2
MD12-3417	Unit 1	3431,5	332,87	1,093	1,027	1,129	0,531	76,2	3,1	345,6	10,5	182,4	79
MD12-3417	Unit 1	3437,4	272,32	1,139	1,005	1,165	0,922	84,2	0,4	354,2	4,2	179,3	85,7
MD12-3417	Unit 1	3443,4	265,01	1,154	1,003	1,182	0,961	79,9	0,9	349,9	2,2	192,9	87,6
MD12-3417	Unit 1	3449,3	291,18	1,165	1,003	1,194	0,96	88,4	0,8	358,3	4,7	188,4	85,2
MD12-3417	Unit 1	3455,2	304,43	1,165	1,002	1,194	0,97	350,4	4,2	80,4	0,3	173,9	85,8
MD12-3417	Unit 1	3461,1	247,14	1,128	1,002	1,15	0,973	118,5	1,3	28,8	4,5	224,7	85,4
MD12-3417	Unit 1	3467	231,51	1,111	1,005	1,132	0,912	31,2	1,3	1,1	3,2	203	86,6
MD12-3417	Unit 1	3473	253,91	1,091	1,014	1,115	0,75	101,6	3,2	11,6	1,6	255,4	86,5
MD12-3417	Unit 1	3479,5	268,41	1,105	1,003	1,124	0,937	120,1	4,8	29,8	4,4	258	83,5
MD12-3417	Unit 1	3488,9	292,73	1,096	1,007	1,116	0,858	10,6	2,5	101	10,1	266,8	79,6
MD12-3417	Unit 1	3496	252,65	1,136	1,001	1,159	0,984	228,3	2,6	318,5	4,2	106,1	85
MD12-3417	Unit 1	3507,9	328,53	1,154	1,004	1,18	0,945	165,6	0,4	75,6	1,5	269	88,5
MD12-3417	Unit 1	3513,8	395,15	1,175	1,017	1,217	0,808	315,5	5,6	45,9	4,3	173,3	82,9
MD12-3417	Unit 1	3519,7	431,99	1,167	1,022	1,212	0,754	322	9,3	52,5	3,1	160,4	80,2
MD12-3417	Unit 1	3525,7	511,46	1,165	1,023	1,21	0,744	306,9	6,8	38,8	14,9	193,1	73,5
MD12-3417	Unit 1	3531,6	476,05	1,155	1,017	1,194	0,785	313	12,4	44,9	8,5	168,5	74,9
MD12-3417	Unit 1	3537,5	264,85	1,111	1,004	1,131	0,927	343,6	3,2	73,8	3,1	207,8	85,5
MD12-3417	Unit 1	3543,4	264,94	1,107	1,01	1,132	0,814	26,9	1,3	296,9	0,8	175,6	88,5
MD12-3417	Unit 1	3549,3	302,16	1,096	1,014	1,122	0,731	31,5	1,7	121,6	1,5	253,3	87,7
MD12-3417	Unit 1	3554,1	325,17	1,152	1,004	1,18	0,942	91,3	2,9	1	6	207,1	83,3
MD12-3417	Unit 1	3558,8	306,45	1,08	1,02	1,107	0,596	12,9	1,9	103	4,2	258,9	85,4
MD12-3417	Unit 1	3564,7	384,36	1,111	1,009	1,136	0,835	160,6	0,3	250,7	3	64,3	87
MD12-3417	Unit 1	3573	317,08	1,171	1,005	1,204	0,943	270,3	3,1	0,4	1	108,6	86,7
MD12-3417	Unit 1	3578,9	255,3	1,124	1,002	1,146	0,966	85,7	0,2	355,7	1,9	182,9	88,1
MD12-3417	Unit 1	3584,9	266,68	1,106	1,007	1,129	0,866	98,4	1,8	8,3	2,9	220	86,6
MD12-3417	Unit 1	3590,8	287,03	1,104	1,005	1,124	0,908	159,6	0,1	69,6	4	251,7	86
MD12-3417	Unit 1	3594,3	338,79	1,101	1,013	1,127	0,759	153,8	3,5	63,6	3,5	288,6	85,1
MD12-3417	Unit 1	3600,3	345,86	1,098	1,017	1,126	0,691	133,3	5,1	42,9	4,3	273	83,4

Core name	Unit	Composite depth (cm)	Km (10^{-6} SI)	F	L	Pj	T	K_1 dec	K_1 inc	K_2 dec	K_2 inc	K_3 dec	K_3 inc
MD12-3417	Unit 1	3607,4	352,94	1,088	1,013	1,112	0,727	141	1,3	231,1	3,3	29	86,4
MD12-3417	Unit 1	3612,1	332,32	1,12	1,002	1,141	0,964	205,5	6,5	115,2	2	8	83,2
MD12-3417	Unit 1	3616,8	267,79	1,148	1,011	1,181	0,852	211,5	0,9	301,5	1,4	90	88,4
MD12-3417	Unit 1	3621,6	306,37	1,157	1,007	1,188	0,906	235,4	2,7	325,7	5,1	117,8	84,2
MD12-3417	Unit 1	3626,3	364,96	1,168	1,009	1,204	0,886	297,1	1,5	27,2	5,8	192,3	84
MD12-3417	Unit 1	3632,2	579,29	1,231	1,012	1,28	0,889	306,2	0,6	36,3	7,6	211,3	82,4
MD12-3417	Unit 1	3634,6	498,15	1,177	1,019	1,222	0,792	312	7,3	45,9	5,4	172,1	80,9
MD12-3417	Unit 1	3641,7	285,1	1,129	1,002	1,151	0,97	108,2	3,9	17,9	3,8	243,3	84,5
MD12-3417	Unit 1	3650	215,7	1,164	1,001	1,192	0,932	284,6	0,6	14,7	2,2	178,2	87,7
MD12-3417	Unit 1	3659,5	255,87	1,098	1,001	1,115	0,957	295,5	1,2	25,6	3	182,7	86,8
MD12-3417	Unit 1	3668,3	305,53	1,122	1,014	1,152	0,791	262	3,9	352,6	9,9	150,9	79,3
MD12-3417	Unit 1	3674,3	261,78	1,083	1,01	1,103	0,773	264,8	3,3	355,1	5,1	141,9	83,9
MD12-3417	Unit 1	3680,2	263,69	1,079	1,014	1,101	0,688	26,5	1,5	296,4	3,2	141,4	86,4
MD12-3417	Unit 1	3686,1	303,99	1,169	1,007	1,132	0,868	25,2	0,8	295,2	0,7	160,7	88,9
MD12-3417	Unit 1	3692	306,14	1,122	1,004	1,145	0,939	116,4	2,3	26,3	2,4	251	86,7
MD12-3417	Unit 1	3697,9	390,25	1,112	1,011	1,139	0,81	115,6	3,9	25,1	7	234,9	82
MD12-3417	Unit 1	3703,9	339,36	1,129	1,017	1,162	0,761	321,1	11,4	51,4	1,3	147,9	78,5
MD12-3417	Unit 1	3709,6	361,5	1,148	1,019	1,187	0,765	295,5	9,1	26,6	7	153,9	78,5
MD12-3417	Unit 1	3715,7	527,29	1,208	1,026	1,264	0,764	312	11,2	44,7	13,3	183,2	72,5
MD12-3417	Unit 1	3721,6	586,98	1,199	1,016	1,245	0,842	299	6,3	30,6	14,5	186,1	74,1
MD12-3417	Unit 1	3727,6	542,97	1,186	1,014	1,228	0,852	56,8	0,2	326,7	2,1	152	87,9
MD12-3417	Unit 1	3733,5	653,76	1,188	1,015	1,232	0,836	247,7	0,1	337,8	5,6	156,3	84,4
MD12-3417	Unit 1	3739,4	264,5	1,13	1,007	1,157	0,887	281,6	1,6	11,7	3,7	168,7	86
MD12-3417	Unit 1	3745,3	281,1	1,145	1,005	1,167	0,929	288	0,5	18,1	4,6	192	85,4
MD12-3417	Unit 1	3751,2	251,65	1,122	1,008	1,147	0,878	86,4	1,1	356,3	3,4	195,1	86,5
MD12-3417	Unit 1	3757,2	294,47	1,113	1,008	1,137	0,864	60,5	2,8	330,4	1,2	216,9	87
MD12-3417	Unit 1	3763,1	282,32	1,107	1,003	1,127	0,947	83,6	3,5	353,6	0,5	256,1	86,4
MD12-3417	Unit 1	3769	273,66	1,096	1,011	1,119	0,781	64,8	0,1	334,8	0,8	165,1	89,2
MD12-3417	Unit 1	3774,9	323,84	1,097	1,009	1,12	0,815	240,4	1,5	150,4	2,2	5,2	87,4

Core name	Unit	Composite depth (cm)	Km (10^{-6} SI)	F	L	Pj	T	K_1 dec	K_1 inc	K_2 dec	K_2 inc	K_3 dec	K_3 inc
MD12-3417	Unit 1	3780,8	331,25	1,137	1,006	1,164	0,911	237,4	0,6	327,4	1,5	124,6	88,3
MD12-3417	Unit 1	3786,8	353,95	1,12	1,005	1,143	0,922	358,6	2,8	88,7	0,3	184,2	87,2
MD12-3417	Unit 1	3792,7	391,65	1,122	1,017	1,155	0,744	326,4	2,1	56,6	6,1	217,3	83,5
MD12-3417	Unit 1	3798,6	431,32	1,18	1,013	1,22	0,856	317	5,2	47,5	5,9	185,6	82,1
MD12-3417	Unit 1	3804,5	480,55	1,192	1,022	1,241	0,782	316,7	5,5	47,9	12,6	203,7	76,2
MD12-3417	Unit 1	3810,4	520,2	1,218	1,016	1,267	0,851	294	0,7	24,2	15,3	201,3	74,7
MD12-3417	Unit 1	3816,4	530,42	1,217	1,014	1,265	0,866	107	1,3	16,7	12,9	202,7	77
MD12-3417	Unit 1	3822,3	671,15	1,208	1,01	1,251	0,896	296,9	5,6	28,7	18	190,2	71,1
MD12-3417	Unit 1	3826,4	457,63	1,168	1,022	1,213	0,753	298,7	14,9	107,7	3,9	3,4	74,6
MD12-3417	Unit 1	3837,7	279,39	1,136	1,002	1,16	0,873	274,3	0,1	4,3	0,4	164,3	89,6
MD12-3417	Unit 1	3846,6	313,03	1,13	1,003	1,153	0,856	295,1	1,3	25,1	2	171,1	87,6
MD12-3417	Unit 1	3850,7	322,67	1,157	1,005	1,187	0,936	304,6	1,6	34,8	7	202,1	82,8
MD12-3417	Unit 1	3854,8	344,17	1,138	1,005	1,164	0,932	317,2	1,1	47,4	10,2	221,3	79,8
MD12-3417	Unit 1	3860,8	282,05	1,108	1,004	1,123	0,914	74,4	2,4	344,2	5,1	189,4	84,3
MD12-3417	Unit 1	3866,7	300,17	1,119	1,003	1,141	0,946	75,8	0,4	345,7	5,4	170,2	84,6
MD12-3417	Unit 1	3875	258,86	1,101	1,006	1,122	0,876	44,5	5,1	134,7	1,8	244,5	84,6
MD12-3417	Unit 1	3882,1	281,78	1,076	1,02	1,103	0,58	61,7	0,2	331,7	1,4	158,2	88,6
MD12-3417	Unit 1	3888	304,31	1,108	1,007	1,131	0,87	261,6	3,8	351,7	1,8	107,4	85,8
MD12-3417	Unit 1	3893,9	334,76	1,109	1,008	1,132	0,86	254,1	5,1	344,5	4,6	115,9	83,1
MD12-3417	Unit 1	3899,8	341,28	1,094	1,016	1,121	0,694	240,7	3,3	331	4,8	116,5	84,2
MD12-3417	Unit 1	3905,8	343,22	1,121	1,017	1,154	0,741	232,3	1	322,4	5,4	131,4	84,5
MD12-3417	Unit 1	3911,7	388,01	1,162	1,004	1,193	0,948	1,2	8,6	270,7	3,2	160,5	80,8
MD12-3417	Unit 1	3917,6	363,2	1,144	1,004	1,171	0,939	353,5	5,5	83,6	1,5	189	84,3
MD12-3417	Unit 1	3924,1	282,13	1,126	1,009	1,153	0,864	254,9	2,9	345,1	4,6	133	84,6
MD12-3417	Unit 1	3929,4	313,16	1,089	1,02	1,118	0,617	253,4	0,3	343,4	3,5	159,1	86,5
MD12-3417	Unit 1	3935,4	349,03	1,153	1,014	1,189	0,819	251,5	4	341,8	4,4	118,9	84
MD12-3417	Unit 1	3941,3	467,81	1,166	1,011	1,202	0,863	327,8	11,8	58,2	2,1	158,2	78
MD12-3417	Unit 1	3944,8	238,46	1,265	1,025	1,332	0,812	238,4	1,3	328,5	3,1	125,7	86,6
MD12-3417	Unit 1	3953,1	298,29	1,097	1,005	1,116	0,893	65,6	1,2	335,5	3,4	175,4	86,4

Core name	Unit	Composite depth (cm)	Km (10^{-6} SI)	F	L	Pj	T	K_1 dec	K_1 inc	K_2 dec	K_2 inc	K_3 dec	K_3 inc
MD12-3417	Unit 1	3959,1	291,47	1,103	1,014	1,129	0,752	261,7	3	352,4	12,3	158,1	77,4
MD12-3417	Unit 1	3965	296,33	1,086	1,014	1,11	0,704	259,4	3,2	350	11	153,4	78,5
MD12-3417	Unit 1	3970,9	284,48	1,099	1,009	1,121	0,819	257	0,6	347,1	8	162,5	81,9
MD12-3417	Unit 1	3976,8	311,38	1,119	1,007	1,144	0,878	271,6	5,8	2,7	10,6	153,4	77,9
MD12-3417	Unit 1	3982,7	346,91	1,151	1,004	1,178	0,951	7,1	8,6	276,8	2	174	81,2
MD12-3417	Unit 1	3988,7	400,3	1,152	1,007	1,183	0,907	2,7	13,9	272,5	0,9	178,9	76
MD12-3417	Unit 1	3994,6	379,7	1,129	1,007	1,156	0,888	26,1	10	295,7	2,5	191,8	79,7
MD12-3417	Unit 1	4000,5	246,12	1,081	1,006	1,098	0,858	65,3	2,6	335,1	4,4	186,3	84,9
MD12-3417	Unit 1	4006,4	251,45	1,071	1,005	1,086	0,86	256,2	0,6	346,2	4,6	159,1	85,4
MD12-3417	Unit 1	4012,3	310,16	1,131	1,004	1,156	0,939	257,6	0,1	347,6	7,1	166,6	82,9
MD12-3417	Unit 1	4017,1	291	1,122	1,004	1,145	0,928	56,4	0,9	326,3	9,9	151,3	80
MD12-3417	Unit 1	4024,2	270,45	1,1	1,004	1,119	0,913	73,3	3,5	343,2	1,4	230,9	86,2
MD12-3417	Unit 1	4030,1	308,85	1,126	1,004	1,149	0,933	56,8	0,5	326,8	4,1	153,9	85,8
MD12-3417	Unit 1	4036	344,97	1,129	1,002	1,153	0,961	21,2	4	290,9	4,5	152,4	84
MD12-3417	Unit 1	4041,9	286,05	1,127	1,006	1,152	0,912	30,9	0,3	300,9	5,9	124,3	84,1

Declaration of interests

☒ The authors declare that they have no known competing financial interests or personal relationships that could have appeared to influence the work reported in this paper.

☐The authors declare the following financial interests/personal relationships which may be considered as potential competing interests:

Highlights

- The AMS makes it possible to distinguish turbidites from hemipelagic sediments.
- Turbidite sequences have very strong degree of anisotropy (Pj).
- Magnetic susceptibility record fluctuates in phase with sediment grain-size.
- Magnetic minerals identified by LT-SIRM are magnetite, hematite and goethite.